JACS
JOURNAL OF THE AMERICAN CHEMICAL SOCIETY
Perspective
pubs.acs.org/JACS

# Strongly Coupled Inorganic/Nanocarbon Hybrid Materials for Advanced Electrocatalysis

Yongye Liang,[†,‡] Yanguang Li,[†] Hailiang Wang,[†] and Hongjie Dai*[,†]

[†]Department of Chemistry, Stanford University, Stanford, California 94305, United States

[‡]Department of Chemistry, South University of Science and Technology of China, Shenzhen 518055, China

**ABSTRACT:** Electrochemical systems, such as fuel cell and water splitting devices, represent some of the most efficient and environmentally friendly technologies for energy conversion and storage. Electrocatalysts play key roles in the chemical processes but often limit the performance of the entire systems due to insufficient activity, lifetime, or high cost. It has been a long-standing challenge to develop efficient and durable electrocatalysts at low cost. In this Perspective, we present our recent efforts in developing strongly coupled inorganic/nanocarbon hybrid materials to improve the electrocatalytic activities and stability of inorganic metal oxides, hydroxides, sulfides, and metal−nitrogen complexes. The hybrid materials are synthesized by direct nucleation, growth, and anchoring of inorganic nanomaterials on the functional groups of oxidized nanocarbon substrates including graphene and carbon nanotubes. This approach affords strong chemical attachment and electrical coupling between the electrocatalytic nanoparticles and nanocarbon, leading to nonprecious metal-based electrocatalysts with improved activity and durability for the oxygen reduction reaction for fuel cells and chlor-alkali catalysis, oxygen evolution reaction, and hydrogen evolution reaction. X-ray absorption near-edge structure and scanning transmission electron microscopy are employed to characterize the hybrids materials and reveal the coupling effects between inorganic nanomaterials and nanocarbon substrates. Z-contrast imaging and electron energy loss spectroscopy at single atom level are performed to investigate the nature of catalytic sites on ultrathin graphene sheets. Nanocarbon-based hybrid materials may present new opportunities for the development of electrocatalysts meeting the requirements of activity, durability, and cost for large-scale electrochemical applications.

## 1. INTRODUCTION

Nowadays, we have become more reliant on energy for every aspect of life than any time in the past. The global demand for energy has been increasing rapidly and continuously. It is projected that the primary energy demand in 2035 could be about 1.5 times of that in 2008.[1] However, until now a significant portion (over 80% in 2008)[2] of the total energy supply comes from fossil fuels, such as coal, oil, and natural gas, which are unsustainable and have finite reserves. The supply and demand issues have caused energy to become one of the greatest challenges facing mankind.

Chemistry as a fundamental science to understand matters in the world and beyond undoubtedly will play important roles in meeting the energy challenges. A great example is electrochemistry that studies the conversion between electricity and energy stored in chemical bonds. Electrochemistry can offer solutions to energy challenges in several ways. First, electrochemical energy conversion is based on chemical reactions at interface, allowing high thermodynamic efficiency in energy conversion.[3] The theoretical efficiency of an electrochemical fuel cell system is much higher than a conventional heat engine limited by Carnot efficiency at low temperature (Figure 1). Second, electrochemical systems can be utilized as efficient and stable platforms for energy conversion and storage, which could be coupled to renewable energy harvesting systems that are temporal in nature and uneven in distribution, such as solar, tidal, and wind. Third, energy conversion in an electrochemical process is a direct and clean process with little impact to the environment, avoiding the pollution and climate change issues currently raised by fossil fuel combustion.[4]

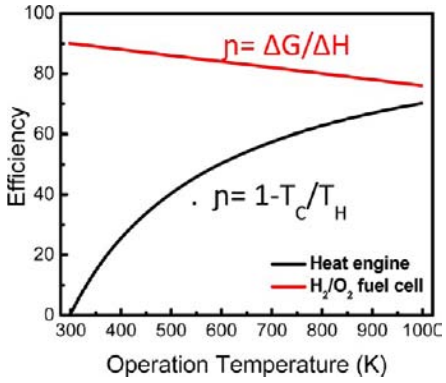

**Figure 1.** Comparison of energy conversion efficiency in a heat engine and $H_2$−$O_2$ electrochemical fuel cell.[5]

In practice, energy conversion in electrochemical processes is often limited by high-activation barriers, which requires extra energy to overcome. The extent of the barrier is defined by overpotential or faradic efficiency. High overpotential or low faradic efficiency will lead to waste of energy to heat. Electrocatalysts are always applied to modify electrode, in order to lower activation energy and increase conversion rate. The performance of electrocatalyst could limit the properties of an electrochemical system, such as energy efficiency, rate

**Received:** September 10, 2012
**Published:** January 22, 2013

dx.doi.org/10.1021/ja3089923 | *J. Am. Chem. Soc.* 2013, 135, 2013−2036

capacity, lifetime, and cost, which makes it a key component of efficient electrochemical conversion. For large-scale applications in energy conversion and storage, electrocatalysts should be efficient, durable, low-cost, and sustainable. However, most of the existing electrocatalysts fall short in one or more of these requirements for some of the most basic but important electrochemical reactions. Precious metal-based materials are a dominant class of electrocatalyst for important energy related electrochemical conversions including oxygen reduction reaction (ORR), oxygen evolution reaction (OER), hydrogen oxidation reaction (HOR), and hydrogen evolution reaction (HER), owing to their high performance and stability.[6] However, the scarcity and consequently high cost of these precious metals make them questionable for large scale applications. Other alternatives based on lower cost materials have been widely explored. However, most of the nonprecious metal catalysts developed still underperform precious metal counterparts. Strategies to develop new materials and/or improve the electrocatalytic activity and stability of existing materials are highly desirable.

This Perspective presents our recent efforts on developing strongly coupled inorganic/nanocarbon hybrid materials for advanced electrocatalysts. Several important electrochemical reactions on energy conversion and storage and their electrocatalyst systems will be briefly reviewed, followed by our motivation and a brief historical account of our efforts in developing inorganic/nanocarbon hybrid materials. We describe our general methods to synthesize strongly coupled inorganic/nanocarbon hybrids and highlight several important examples of these hybrid materials for ORR, OER, and HER electrocatalysis. Beyond synthesis and electrochemical properties, characterization of the structures of the hybrid materials and nature of coupling between inorganic nanoparticle and nanocarbon will be discussed. Instead of an exhaustive review of the field, this Perspective will aim at demonstrating the promising opportunities presented by strongly coupled inorganic/nanocarbon hybrid materials for electrocatalysis and provide a guideline for both fundamental understandings and practical applications of these materials.

## 2. ELECTROCATALYST FOR ENERGY CONVERSION AND STORAGE

Energy conversion and storage can be performed through electrochemical processes especially those involving ORR, OER, HOR, and HER. Below, we will briefly introduce these reactions and electrocatalysts used for them.

**2.1. Oxygen Reduction Reaction (ORR).** ORR (Figure 2) is the cathode reaction for a range of energy applications including fuel cells, metal-air batteries, and chlor-alkali electrolysis.[7] The strong O═O bond makes ORR difficult to proceed, which requires four coupled electron and proton transfers. Therefore, ORR is kinetically very sluggish. Various materials have been investigated as catalysts to enhance ORR. Platinum-based materials (Pt and its alloys) are most widely used catalysts for ORR with low overpotential and good stability[8] but come at a price of high cost and scarcity.[8c] Low-cost alternatives, such as metal-N complex on carbon matrices (M-N/C),[9] metal chalcogenides,[10] perovskites,[11] spinel oxides,[12] and doped carbonaceous materials[13] have been explored with promising advances.[9a,c] Despite of these advances, it is still challenging to develop ORR catalysts with high activities comparable to Pt-based materials, similar or higher stability than Pt-based materials and at much lower cost. Thus far, the cathode oxygen electrocatalyst has been one of the major limiting factors for energy conversion efficiency, cost, and stability of fuel cells and metal-air batteries.[14]

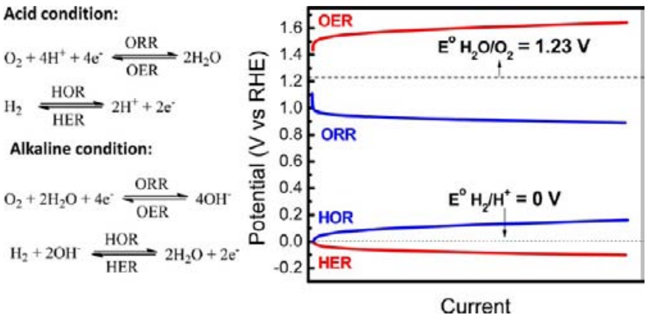

**Figure 2.** ORR, OER, HOR, and HER and their representative polarization curves.

**2.2. Oxygen Evolution Reaction (OER).** OER is the process to generate $O_2$ through electrochemical oxidation of water, which is a half reaction of water splitting and solar fuel synthesis[15] and is also involved in the charging process of rechargeable metal-air batteries.[16] As the reverse reaction of ORR, OER also proceeds through multistep proton-coupled electron transfer and is kinetically sluggish.[17] An effective electrocatalyst is needed in order to expedite the reaction, reduce the overpotential, and thus enhance the energy conversion efficiency. Currently, the most active OER catalysts are $RuO_2$ or $IrO_2$ in acidic or alkaline solutions,[15a,18] but these catalysts suffer from the scarcity and high cost of precious metals. Extensive efforts have been taken to develop highly active, durable and low cost alternatives, such as first-row transition-metal oxides[19] and perovskites.[20]

**2.3. Hydrogen Evolution Reaction (HER) and Hydrogen Oxidation Reaction (HOR).** Hydrogen is a promising energy carrier to replace hydrocarbon due to its cleanness and ease of production. HER is the process to produce $H_2$ from water, store electrical energy in the form of $H_2$, which is the cathodic half reaction in water splitting. HOR, the reverse reaction to convert $H_2$ into electricity, is the anode reaction in $H_2$−$O_2$ fuel cell. Compared to oxygen electrode reaction, both HER and HOR only involves two electron transfers, affording faster reaction kinetics.[21] Generally, a good catalyst for HER is also a good catalyst for HOR. Pt-based electrocatalyst is the most effective and practical electrocatalyst thus far for both HOR and HER with rather small overpotential. However, besides the price and supply issues, Pt-based materials are readily poisoned by carbon monoxide existing in the reformate $H_2$ gas and byproduct of alcohol oxidation in the case of direct alcohol fuel cells.[22] More economical electrocatalysts based on non-noble metal are explored recently, including transition-metal chalcogenides,[23] carbides,[24] complex[25] and metal alloys,[26] although they are still less effective or stable than Pt-based electrocatalyst.

The reactions discussed above are central to the area of electrochemical energy conversion and storage, especially for renewable energy sources. In addition, there are also other reactions important to the field. Alcohol oxidation reaction is analogous to hydrogen oxidation, which can be coupled to the anode of fuel cells.[27] Compared to hydrogen, small-chain alcohols are easy to store and transport. Pt or Pt-based alloys are traditional electrocatalysts for alcohol oxidation. Electrochemical reduction of $CO_2$ is the conversion of $CO_2$ to lower valence fuel species. The reaction enables the closing of anthropogenic carbon cycle by electricity using renewable energy. Currently, there are no electrocatalyst systems that are efficient and stable enough for practical application of $CO_2$ reduction.[28]

In terms of catalyst synthesis, conventional Pt electrocatalysts are typically formed and supported on conductive carbon black with high surface area (Figure 3).[29] Carbon support can increase the dispersion and utilization of the active catalyst, so that catalytic activity could be improved. Meanwhile, interactions between carbon support and metal can further enhance the stability of catalyst.[30] Carbon support is also needed for nonprecious metal-based electrocatalyst, especially for those with low electrical conductivity. Carbon support can provide paths for the flow of electrons in the electrocatalytic system.

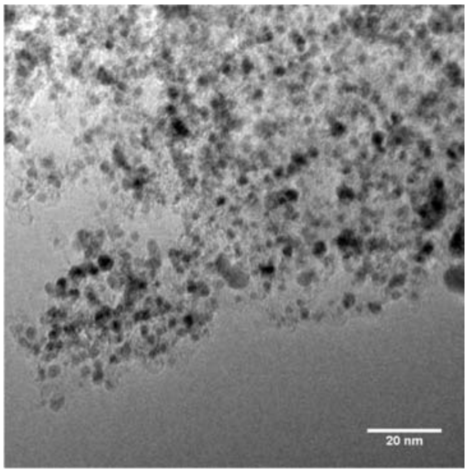

**Figure 3.** TEM image of Pt/Vulcan XC-72.

The electrodes of many nonprecious metal electrocatalysts are typically prepared by mixing electrocatalysts with carbon black. However, simple mixing affords limited interactions between the electrocatalyst and the carbon, leaving a significant portion of the material electrochemically inactive.[31] Direct synthesis or coating of electrocatalysts on carbon supports was also studied,[31,32] but the catalytic activities of these hybrids/composites were not optimized due to excessive oxidation of the carbon or the weak oxide-carbon coupling. An ideal carbon material to couple with electrocatalyst requires high surface area and high electrical conductivity as well as sufficient functional groups on carbon to afford intimate interactions with inorganic materials. Such interactions could also lead to high durability and chemical stability of the catalyst to resist corrosion.[30]

## 3. ACCOUNT OF OUR WORK ON STRONGLY COUPLED INORGANIC/NANOCARBON HYBRIDS

In the past several years, our group has developed synthesis of graphene and carbon nanotube (CNT) hybrid nanomaterials for electrocatalysts.[33] Such hybrid materials contain inorganic nanoparticles selectively nucleated and grown on the oxygen functional groups of nanocarbon, which differs from typical electrocatalysts prepared by mixing active inorganic materials with a certain form of carbon. This relatively new research direction in our group was initially motivated by experimental observations made in our earlier work of coating CNTs and graphene with metal or metal oxide dielectric layers for electronic devices,[34] briefly reviewed below.

Our earlier work since 2000 has found that since pristine CNTs and graphene are chemically inert, it is difficult to attach metal or metal oxide nanoparticles onto them without chemical

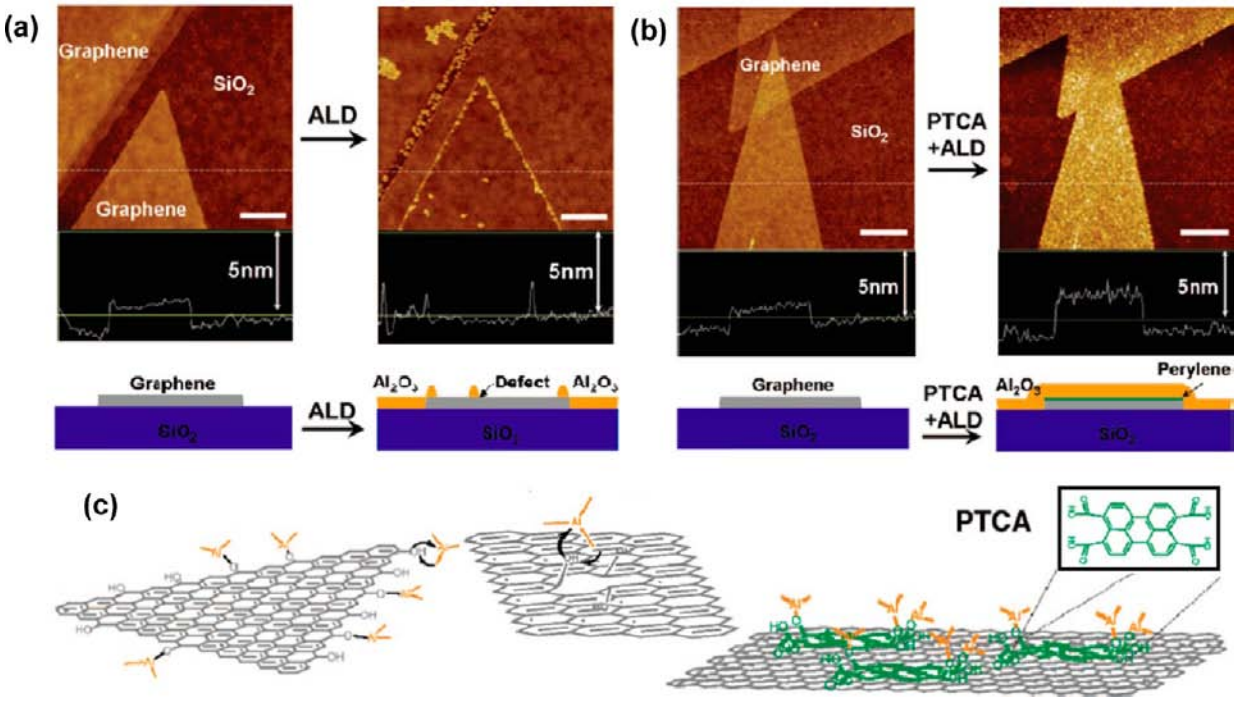

**Figure 4.** Synthesis of $Al_2O_3$ /graphene hybrid. (a) ALD of $Al_2O_3$ on pristine graphene, scale bar is 200 nm. (b) ALD of $Al_2O_3$ on PTCA-coated graphene, scale bar is 500 nm. (c) Schematics of $Al_2O_3$ deposition on various graphene substrates. Reproduced with permission from ref 34c. Copyright 2008 American Chemical Society.

functionalization to impart functional groups by surfactant, nucleic acid or polyaromatic molecules.[34] For instance, in 2008, we investigated the growth of $Al_2O_3$ on graphene sheet by atomic layer deposition (ALD) method.[34c] We found that instead of uniform coating on pristine graphene sheets, $Al_2O_3$ mostly grew on edges and defect sites (Figure 4), suggesting that the chemical groups on the edge and defect sites acted as nucleation, growth, and anchoring site to interact with ALD precursors, while the basal plane of pristine graphene lacked such interactions, even though it had high surface area. To enhance nucleation and growth, we used perylene tetracarboxylic acid (PTCA) to functionalize the graphene sheets. The perylene core could interact with the basal plane of graphene through $\pi$–$\pi$ interaction, while the carboxylic acid groups could interact and react with the ALD precursors. The resulting PTCA functionalized graphene could be uniformly coated with ultrathin $Al_2O_3$ layer over a large area (Figure 4). This result suggested the importance of functionalization of graphene for the growth of metal oxides.

The research above marked the beginning of our effort to synthesize inorganic nanoparticles, nanoplates, and nanorods on graphene and CNTs that were oxidized to various degrees with different amounts of oxygen functional groups. Our motivation was that nucleation and growth of electrically insulating metal oxides, hydroxides, and sulfides on graphene and CNT with controlled oxidation should afford the best electrical wiring to the inorganic nanomaterials, fully utilizing the high electrical conductivity, large surface area, high mechanical strength, and structural flexibility of nanocarbon.[35] This approach could produce advanced hybrid and composite materials for various electrochemical applications, such as electrodes for supercapacitor, lithium ion batteries, and electrocatalysts.

Indeed, in most cases, we found that the direct growth or anchoring nanocrystals on graphene oxide (GO) sheets or oxidized CNTs (oxCNT) afforded formation of strongly coupled hybrid (SC-hybrid) materials with optimal electrical and mechanical coupling. Compared to electrode materials based on physical mixtures of inorganics and nanocarbon, the SC-hybrid exhibited either higher capacity/capacitance, enhanced charging/discharging rate capability, higher catalytic activity, and/or improved cycling stability, leading to high-performance batteries,[36] supercapacitors,[37] fuel cell,[33b−e] and water splitting electrocatalysts,[33a,b] and other types of energy storage and conversion materials.

For example, we developed a two-step method to grow $Ni(OH)_2$ nanocrystals on graphene oxidized to various degrees by potassium permanganate and explored their properties for electrochemical pseudocapacitors (Figure 5a).[37a] The crystalline $Ni(OH)_2$ nanoplates grown on mildly oxidized graphene sheets (GS) formed an electrochemical pseudocapacitor electrode with a stable capacitance of ~900 F/g at a high discharge current density of 40 A/g (Figure 5b), which was almost twice of the capacitance made by simple mixing of $Ni(OH)_2$ nanoplates with graphene. In another work, $Mn_3O_4$ nanoparticles were grown selectively on reduced graphene oxide (rGO) sheets to afford wiring of electrically insulating $Mn_3O_4$ nanoparticles to current collectors through the underlying network of conducting graphene sheets (Figure 5c).[36a] The $Mn_3O_4$/graphene hybrid as an anode material in lithium batteries showed a high specific capacity up to ~900 mAh/g with good rate capability and cycling stability, which substantially outperformed physical mixtures of $Mn_3O_4$ nanoparticles and graphene (Figure 5d).

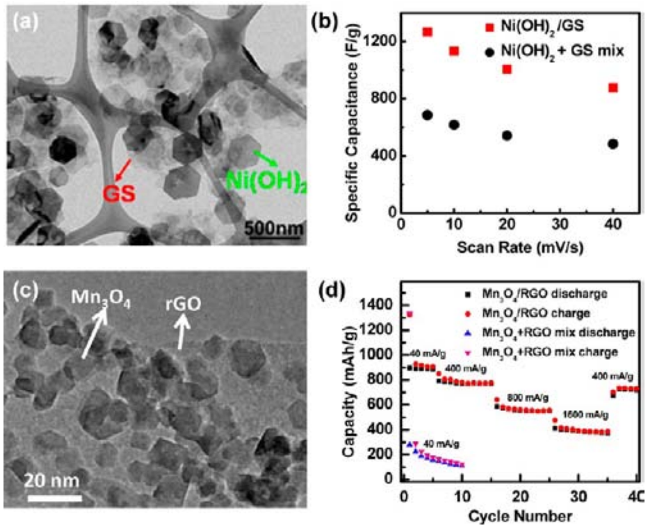

**Figure 5.** (a) TEM image of the $Ni(OH)_2$/GS hybrid. (b) Average specific capacitance of the $Ni(OH)_2$/GS hybrid and $Ni(OH)_2$ + GS mixture at various scan rates. Reproduced with permission from ref 37a. Copyright 2010 American Chemical Society. (c) TEM image of the $Mn_3O_4$/rGO hybrid. (d) Capacity retention of the $Mn_3O_4$/rGO hybrid and $Mn_3O_4$ + rGO mixture at various current densities. Reproduced with permission from ref 36a. Copyright 2010 American Chemical Society.

Extending the concept above, we recently developed a new type of Ni−Fe battery by employing strongly coupled inorganic nanoparticle/nanocarbon hybrid materials for making the two opposing electrodes in aqueous batteries (Figure 6a).[36c] We found that when pairing $Ni(OH)_2$/CNT and $FeO_x$/graphene hybrid materials together, one could deliver nearly 1000 times faster charge and discharge rates compared to traditional Ni−Fe batteries without obvious loss of specific capacity. As a result, such inorganic nanoparticle/nanocarbon hybrid battery delivered energy density similar to traditional Ni−Fe batteries but much higher power density similar to supercapacitors (Figure 6b,c).[36c] Direct growth of electrochemically active inorganic nanomaterials on mildly oxidized nanocarbon materials affords strong chemical and electrical coupling between inorganic nanoparticles and carbon, allowing for rapid electron transfer from active materials to current collectors. Thus, this approach could open a venue toward batteries with ultrafast charge and discharge capabilities while attaining energy densities close to the theoretical limit.

Our work on electrocatalyst started with a serendipitous observation that a $Co_3O_4$/graphene hybrid was highly active for ORR, although the original goal of synthesizing such material was for lithium ion battery electrode much like the $Mn_3O_4$/graphene hybrid.[36a] Indeed, due to the desirable electrical and mechanical properties, combined with high surface area and rich functionality, oxidized graphene and CNT could be exploited to derive advanced electrocatalysts.[1] Several recent papers have reported using CNT or graphene as support for Pt (or Pd) in ORR catalyst application.[2,38] The graphene or CNT support showed improved activity and stability compared to other carbon-based supports. Nitrogen-doped CNTs or graphene sheets prepared by high-temperature methods have also been reported to show moderate catalytic activities for ORR.[13a,31,39]

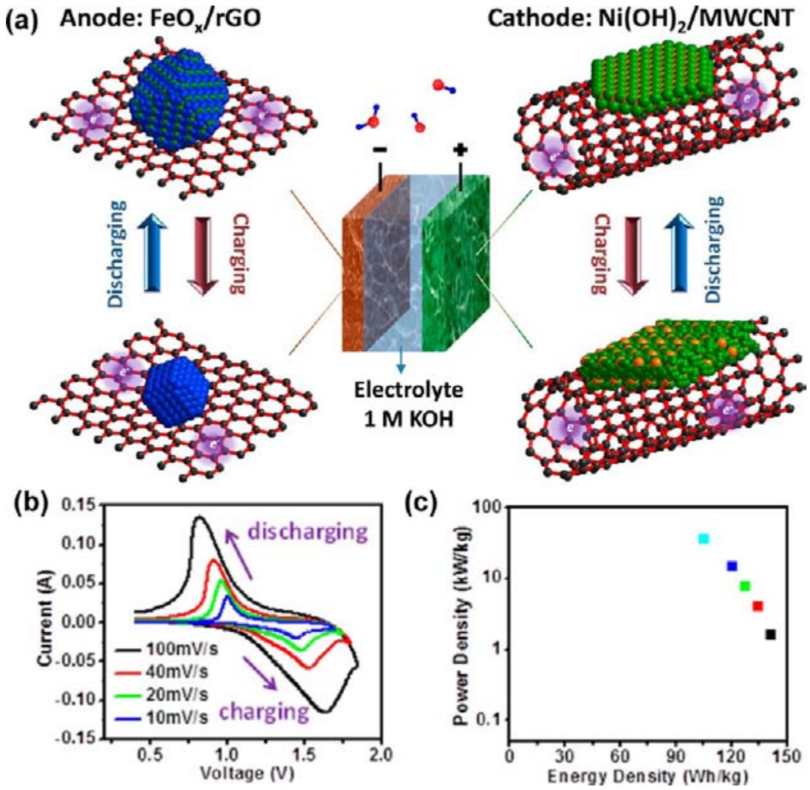

**Figure 6.** (a) Scheme of the ultra-Ni−Fe battery made from inorganic nanoparticle/nanocarbon hybrid materials. An FeO$_x$/rGO hybrid was used as the anode and a Ni(OH)$_2$/MWCNT hybrid was used as the cathode. Upon charging, Ni(OH)$_2$/MWCNT and FeO$_x$/graphene were converted to NiOOH/MWNT and Fe/graphene, respectively. Upon discharging, NiOOH/MWCNT and Fe/graphene were converted back to Ni(OH)$_2$/MWCNT and FeO$_x$/graphene, respectively. (b) CV curves at various scan rates in two electrode configuration in 1 M KOH. 1.1 mg of Ni(OH)$_2$/MWCNT and 0.7 mg of FeO$_x$/graphene were loaded into 1 cm$^2$ Ni foams to form the electrodes. (c) Ragone plot of the ultra-Ni−Fe battery measured in charging at 3.7A/g from 0.4 to 1.67 V. Reproduced with permission from ref 36c. Copyright 2012 Nature Publishing Group.

Cobalt-based spinel oxides have been widely investigated as electrocatalysts.[40] In particular, $Co_3O_4$ has been shown to exhibit excellent OER catalytic activities in alkaline condition.[41] However, the performance limit of $Co_3O_4$-based materials in terms of activity and stability for ORR has not been well established in the literature. We synthesized a hybrid material of $Co_3O_4$ nanocrystals grown on reduced, mildly oxidized graphene oxide (rmGO) (Figure 7a)[33b] and observed improved OER activity of $Co_3O_4$ over free $Co_3O_4$ nanoparticles physically mixed with rmGO, suggesting improved OER electrocatalytic activity of the hybrid material (Figure 7b). Interestingly, when we extended the voltage scan window to a more negative region, the $Co_3O_4$/rmGO hybrid also exhibited a higher oxygen reduction current density than the physical mixture from cyclic voltammetry (CV) measurement (Figure 7c). While free $Co_3O_4$ particles and rmGO each separately exhibited catalytic activity for ORR, the $Co_3O_4$/rmGO hybrid afforded smaller overpotential and higher peak current for ORR, indicating a synergistic effect in electrocatalysis (Figure 7c). The high ORR activity of the $Co_3O_4$/rmGO hybrid was intriguing and inspired us to pursue strongly coupled inorganic/nanocarbon hybrids for electrocatalysis, as detailed in later sections after a brief review of the synthesis methods.

## 4. SYNTHESIS OF STRONGLY COUPLED INORGANIC/NANOCARBON HYBRIDS

### 4.1. Oxidation and Functionalization of Nanocarbon Materials.

Surface functionalization of carbon atom lattices is important to synthesize inorganic nanocrystal/graphene or inorganic/CNT hybrids.[34,42] The functionalization could be categorized by noncovalent and covalent methods. In the noncovalent method, surfactants or modified molecules are introduced to interact with graphene or CNTs through noncovalent bonds, such as $\pi-\pi$ stacking and hydrophobic wrapping.[34] Covalent modification methods utilize chemical functionalization through oxidation,[43] cycloaddition,[44] or radical addition.[45] Due to high efficiency and simplicity, functionalization by oxidation to introduce oxygen functional groups in graphene to form graphene oxide (GO) or oxCNT is the most effective way to prepared inorganic/nanocarbon hybrids.

GO sheets are most often prepared by the Hummers method.[46] In this method, a mechanically grounded graphite powder is treated in sulfuric acid and oxidized by potassium permanganate. GO sheets are obtained after washing and sonication to form a stable suspension in an aqueous solution. The Hummers method offers a high yield of GO sheets, but the graphitic lattice in GO sheets is damaged and contains abundant functional groups including hydroxyls, epoxides, carbonyls, and carboxyl acid groups.[47] This leads to the substantial reduction of the electrical conductivity of graphene sheet, even after postreduction treatment. To circumvent this problem, we developed a simple method to synthesize GO sheets with controlled degree of oxidation by adjusting the amount of potassium permanganate used in Hummers method.[48] For example, a mildly oxidized graphene oxide (mGO) was prepared by using 6 times lower concentration of $KMnO_4$ to result in GO sheets with lower oxygen content than

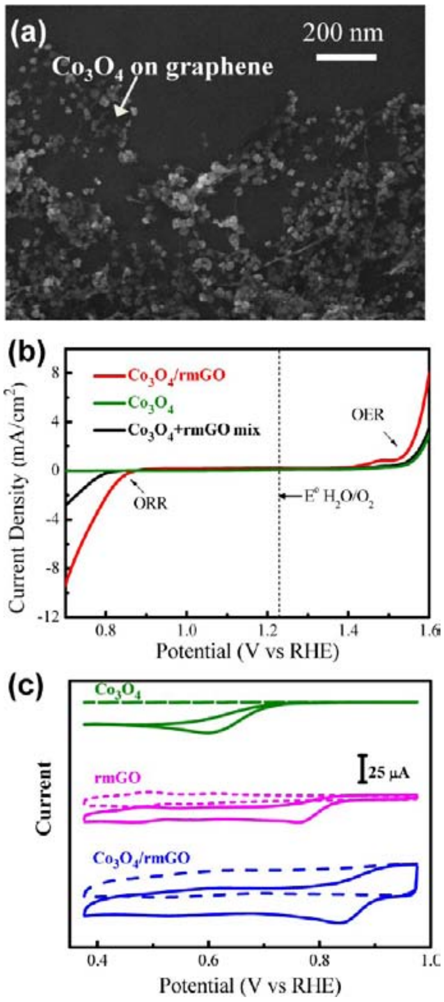

**Figure 7.** (a) SEM image of the $Co_3O_4$/rmGO hybrid. (b) Oxygen electrode activities within the ORR and OER potential window of the $Co_3O_4$/rmGO hybrid, $Co_3O_4$ + rmGO mixture and $Co_3O_4$ nanoparticles (catalyst loading ~0.24 mg/cm$^2$ for all samples) dispersed on carbon fiber paper in $O_2$-saturated 0.1 M KOH. (c) CV curves of $Co_3O_4$ nanoparticles, rmGO, and the $Co_3O_4$/rmGO hybrid, on glassy carbon electrodes in $O_2$-saturated (solid line) or Ar-saturated 0.1 M KOH (dash line). Catalyst loading was 0.17 mg/cm$^2$ for all samples. Reproduced with permission from ref 33b. Copyright 2011 Nature Publishing Group.

Hummers GO (~15% vs ~30% measured by XPS and Auger spectroscopy).[36a] This led to GO sheets with sufficient oxygen functional groups for nucleation and growth of inorganic nanocrystals on GO sheets, while the mGO maintained relatively high electrical conductivity (especially after reduction) needed for electrochemistry. Thus, it is possible to identify an optimal oxidation degree of GO to balance chemical functionality needed for optimal coupling with inorganic particles and high electrical conductivity needed for charge transfer in electrochemical processes.[33b,d,g,37a]

The Hummers oxidation method can be extended to the synthesis of oxCNTs. Compared to the commonly used strong oxidizing acids (like $HNO_3$ and $HNO_3$–$H_2SO_4$) used for CNT oxidation,[42,43] the modified Hummers method can afford milder oxidation conditions and offer easier control on the oxidation degree. High-resolution TEM images revealed that the inner walls of the oxCNT were graphitic and continuous, suggesting that the inner walls were not destroyed or oxidized during the oxidation process.[33g] From XPS measurement, we found the oxCNT prepared by the modified Hummers method had a higher ratio of −COO species to C−O species (9/21%) than that of oxCNTs prepared by refluxing in $HNO_3$ (6/26%), suggesting that the Hummers method was advantageous in producing more abundant −COO species that could serve as nucleation and anchored sites for nanocrystal growth.[33g] Indeed, the type of oxidation method and detailed reaction parameters of oxidation is an important factor in the synthesis of inorganic/nanocarbon hybrids. Different methods or conditions of nanocarbon oxidation could lead to inorganic/nanocarbon hybrid with drastically different properties and must be carefully optimized for each type of inorganic material to be synthesized on oxidized graphene or CNTs.

**4.2. Synthesis of Inorganic/Nanocarbon Hybrid Materials.** It is important to construct inorganic/nanocarbon hybrid materials through nucleation and growth of inorganic nanoparticles selectively on nanocarbon with the help of oxygen functional groups, without free growth in solution. In the past, there have been several reports on the synthesis of inorganic/CNT hybrids or composites, such as $SnO_2$/CNT,[49] $RuO_2$/CNT,[50] and $Co_3O_4$/CNT.[51] However, no systematic work has been done to control the synthesis selectivity, identify the optimal oxidation method, and oxidation degree to balance inorganic-carbon coupling and the electrical properties of CNTs. Also, little has been done to investigate the nature of coupling between inorganic nanomaterials and CNTs.

We have developed a two-step solution or gas-phase synthesis method to produce strongly coupled inorganic nanoparticle/nanocarbon hybrid materials without the formation of free nanoparticles in solution (Figure 8a,b). The first step is the nucleation and growth of inorganic precursor on GO or oxCNT stably suspended in solutions through controlled solution-phase reactions by taking advantage of metal ion coordination with oxygen functional groups followed by hydrolysis.[36a,52] The reaction rate can be fine-tuned by controlling the reaction temperature, solvent composition and other parameters. For example, cosolvents such as alcohols or DMF can be added to aqueous salt solutions to slow down hydrolysis reactions rates. Careful pH control can also be carried out by adding acid or base to control reaction rates. Fine tuning of these parameters allows for selective nucleation of inorganic nanoparticles on GO or oxCNTs, with little particle growth in the free solution.

Once the metal salt precursor species are exhausted in the solution and a uniform coating of GO sheets or oxCNTs by hydrolyzed/reacted products are achieved in the first step, a second step treatment of the intermediate product by hydrothermal (or solvothermal) annealing or gas-phase thermal annealing is applied to crystallize the precursors nucleated on the GO or oxCNTs to form nanocrystals. GO and oxCNT are reduced to some degree in the second step. The temperature and reaction time can be varied to tune the size and crystallinity of the nanocrystals. Hydrothermal (or solvothermal) reactions are known to produce crystalline nanoparticles at relatively low temperatures (<200 °C). Gas-phase thermal annealing or other reactions can prevent overgrowth of nanocrystals by avoiding or limiting Ostwald ripening and can be carried out at much higher temperatures than hydrothermal conditions. It should be pointed out that oxygen functional groups could be removed during the reduction process. As a result, mild reduction treatment should be adopted. Strong reduction treatment could lead to detachment of inorganic nanoparticles from nano-

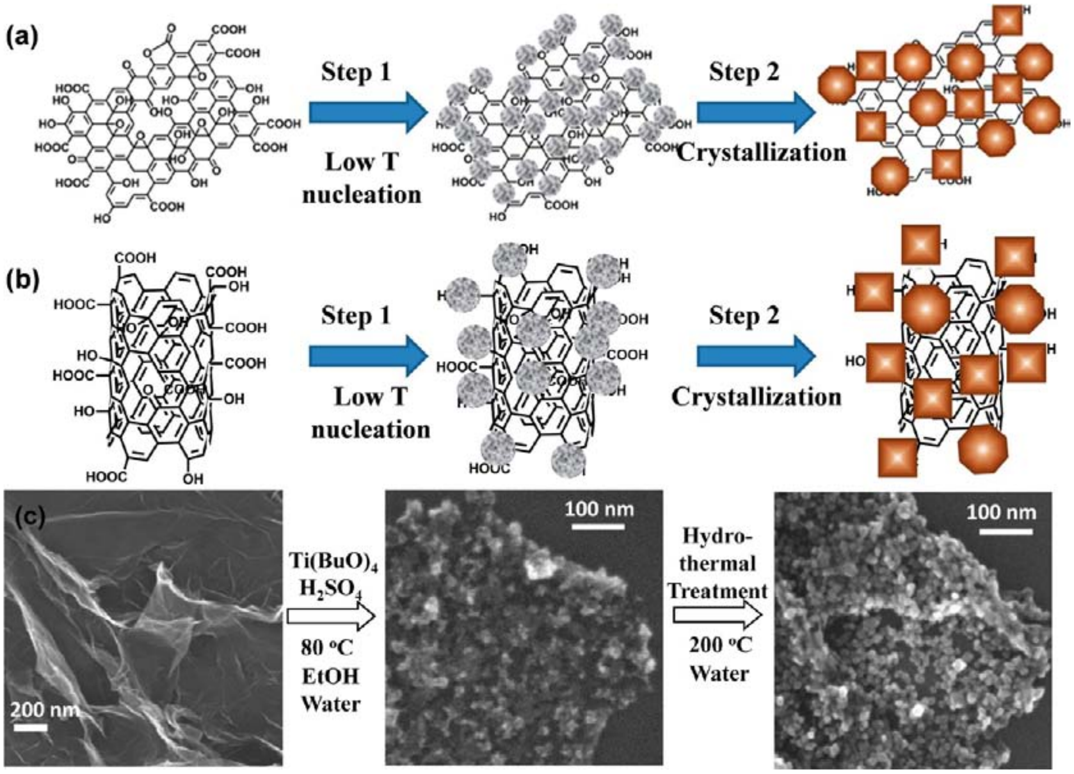

**Figure 8.** Schematic illustration for the synthesis of inorganic nanoparticle/nanocarbon hybrid. The cases of (a) graphene and (b) CNT. (c) An example of the $TiO_2$/rGO hybrid. In the first step, $TiO_2$ nanoparticles grow on GO sheet through controlling hydrolysis of Ti precursor. Such hybrid is transformed to $TiO_2$ nanocrystal/rGO hybrid by hydrothermal treatment in the second step. Reproduced with permission from ref 53. Copyright 2010 Springer.

carbons. For example, we found that inorganic nanoparticles detached from nanocarbons when the hybrids were reduced by hydrazine in solution in the second step.

As a specific example, we review the synthesis of the $TiO_2$/graphene hybrid (Figure 8c). Fine nanoparticles of amorphous $TiO_2$ were coated on GO sheets by hydrolysis of $Ti(BuO)_4$ at 80 °C in a EtOH/$H_2O$ mixed solvent.[53] Addition of $H_2SO_4$ and low water ratio (EtOH/$H_2O$ = 15/1, volume ratio) in the solution was important to slow down the hydrolysis reaction, thus affording selective growth of $TiO_2$ on GO (Figure 8c) with little free growth of $TiO_2$ particles in solution. The average size of $TiO_2$ nanoparticle increased with higher water/EtOH ratio in the first step reaction due to higher hydrolysis reaction rate. Nanoparticles were less tightly bonded to GO sheets, and some free growth of $TiO_2$ particles occurred. This was especially obvious when the synthesis was carried out in pure water (Figure 9). The first step reaction is critical to selective growth of inorganics on GO or oxCNT. In the second step, hydrothermal treatment of the amorphous $TiO_2$/GO at 200 °C was carried out to afford crystallization of $TiO_2$ into anatase nanocrystals selectively on the GO sheets (Figure 8c).[53] UV−vis absorbance spectra showed that the absorption peak of GO was red-shifted after hydrothermal treatment, suggesting the reduction of GO to a certain extent.

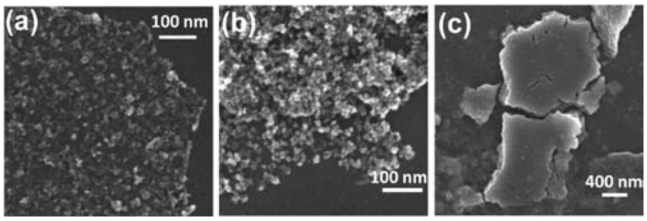

**Figure 9.** SEM images of first step products of the $TiO_2$/GO hybrid prepared by using different EtOH/water ratios of (a) 15:1, (b) 3:1, and (c) 0:1 (volume ratio). Reproduced with permission from ref 53. Copyright 2010 Springer.

Our two-step method is straightforward and general for the synthesis of various types of metal oxide/nanocarbon hybrids. It has also been used for the synthesis of nanocarbon hybrids with metal hydroxides,[54] chalcogenides,[33c] and ternary systems like lithium metal phosphate.[36b] This method can be extended to other complicated systems with proper adjustment of the reaction conditions.

It is interesting to note that synthesis of inorganic nanomaterials on nanocarbon substrate can differ dramatically from growth in solutions free of any GO or oxCNT substrates. Inorganic nanoparticles grown on nanocarbon often afforded smaller particle size and less aggregation than those grown freely in solution by the exact same synthesis method and conditions. This was observed in the cases of manganese oxide,[36a] lithium metal phosphate,[36b] cobalt sulfide,[33c] and molybdenum sulfide.[33a] We have also found for nanomaterials (such as Ni, Co, and Fe hydroxide) nucleated and grown at oxygen functional group sites of GO, the morphology of the nanomaterials could be strongly affected by the oxidation degree of GO.[54] Thus, nucleation and growth on nanocarbon allows for a degree of tuning of the morphology of inorganic nanoparticles to favorable sizes and shapes (such as nanorod)[36b] to facilitate electrochemical processes in batteries and electrocatalysis. This is an important aspect of strongly coupled inorganic/nanocarbon hybrid materials.

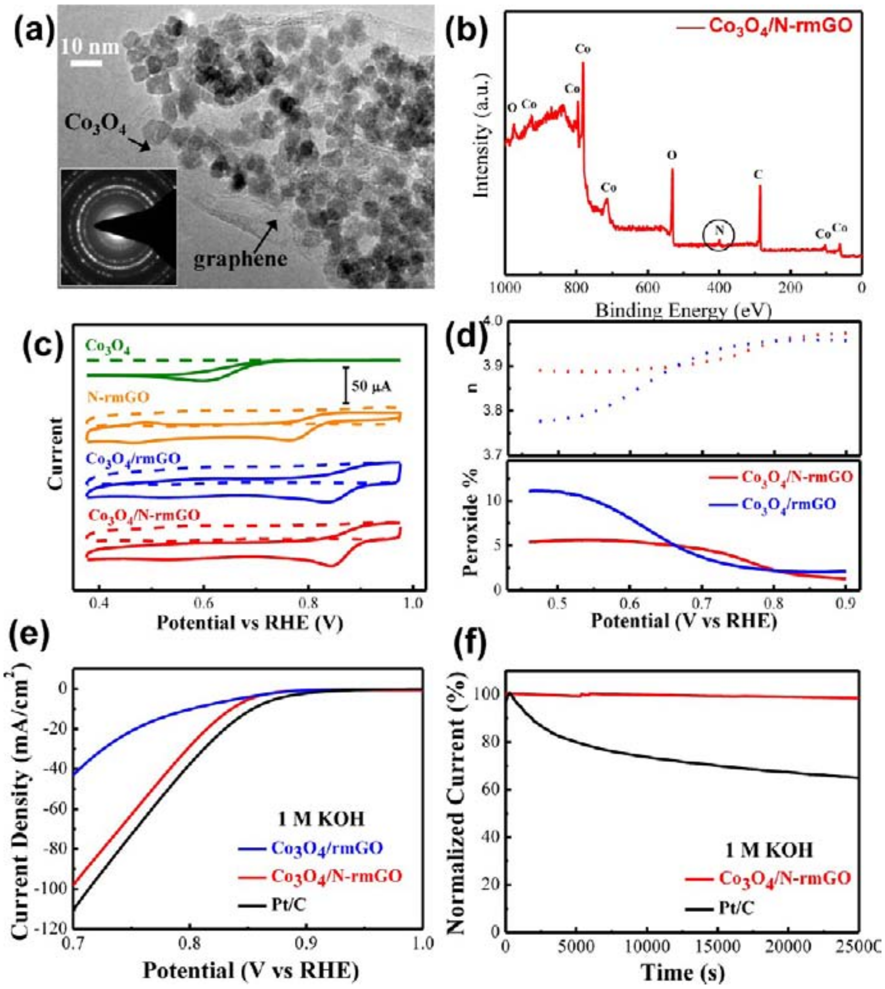

**Figure 10.** (a) TEM images of the $Co_3O_4$/N-rmGO hybrid. The electron diffraction pattern of the $Co_3O_4$ nanocrystals on graphene is showed in inset. (b) An XPS spectrum of the $Co_3O_4$/N-rmGO hybrid. (c) CV curves of the $Co_3O_4$/N-rmGO hybrid, $Co_3O_4$/rmGO hybrid, N-rmGO, and $Co_3O_4$ nanoparticles on glassy carbon electrodes in $O_2$-saturated (solid line) or Ar-saturated 0.1 M KOH (dash line). Catalyst loading was 0.17 mg/cm$^2$ for all samples. (d) Percentage of peroxide (solid line) and the electron transfer number (*n*) (dot line) of the $Co_3O_4$/rmGO and $Co_3O_4$/N-rmGO hybrids at various potentials based on the RRDE data. (e) Oxygen reduction polarization curves of the $Co_3O_4$/rmGO, $Co_3O_4$/N-rmGO hybrids, and a high-quality commercial 20% Pt/C catalyst (catalyst loading ~0.24 mg/cm$^2$ for all samples) dispersed on carbon fiber paper in $O_2$-saturated 1 M KOH. (f) Chronoamperometric responses of the $Co_3O_4$/N-rmGO hybrid and Pt/C on carbon fiber paper electrodes kept at 0.70 V vs RHE in $O_2$-saturated 1 M KOH. Reproduced with permission from ref 33b. Copyright 2011 Nature Publishing Group.

## 5. ELECTROCATALYST FOR ORR IN ALKALINE MEDIA

Oxygen reduction electrocatalysts in alkaline media are useful for various technologies including alkaline fuel cells, metal-air batteries, and chlor-alkali electrolysis.[55] ORRs are known to proceed more readily in alkaline media than in acid media, and there are more choices of ORR electrocatalysts in alkaline media than in acids.[56] Even with a boarder range of materials available, it is still challenging to develop a low-cost ORR electrocatalyst with high activity comparable to Pt and excellent stability and durability in alkaline conditions. The strongly coupled inorganic/nanocarbon hybrid catalyst may offer a solution to this problem.

**5.1. $Co_3O_4$ Nanocrystals Grown on Mildly Oxidized Graphene Sheets.** Using the two-step method described above, we synthesized a hybrid material of $Co_3O_4$ nanocrystals grown on mGO reduced through the hydrothermal steps (rmGO) and observed its high electrocatalytic activity for ORR. We further optimized the hybrid synthesis by adding $NH_4OH$ in the first step. Ammonia can coordinate to Co cation to mediate hydrolysis of $Co^{2+}$ and its oxidation.[57] Not only did the $NH_4OH$ addition yielded smaller $Co_3O_4$ nanocrystals on graphene sheets (Figure 10a), it also provided a source of nitrogen and afforded nitrogen doping on rGO (Figure 10b). Through CV measurements, we observed that the $Co_3O_4$/N-rmGO hybrid was more active than $Co_3O_4$/rmGO with a more positive peak potential and higher peak current density for ORR catalysis (Figure 10c). Rotating ring-disk electrode (RRDE) measurements suggested that the ORR pathway catalyzed by both the $Co_3O_4$/N-rmGO and $Co_3O_4$/rmGO hybrids was mainly 4*e* reduction, yielding low amounts of peroxide species (Figure 10d).

We further measured the *iR*-compensated polarization curves on Teflon-treated carbon fiber paper (TCFP), which was close to the setup of real fuel cell. The porous TCFP substrate is highly hydrophobic, providing three phase contact points for oxygen, electrolyte, and catalyst. Therefore, the measured current on TCFP is not as limited by oxygen concentration in the electrolyte as on other substrates and can better reflect the kinetic property of the catalyst loaded.[58] At the same mass loading of catalysts, the $Co_3O_4$/N-rmGO hybrid showed just

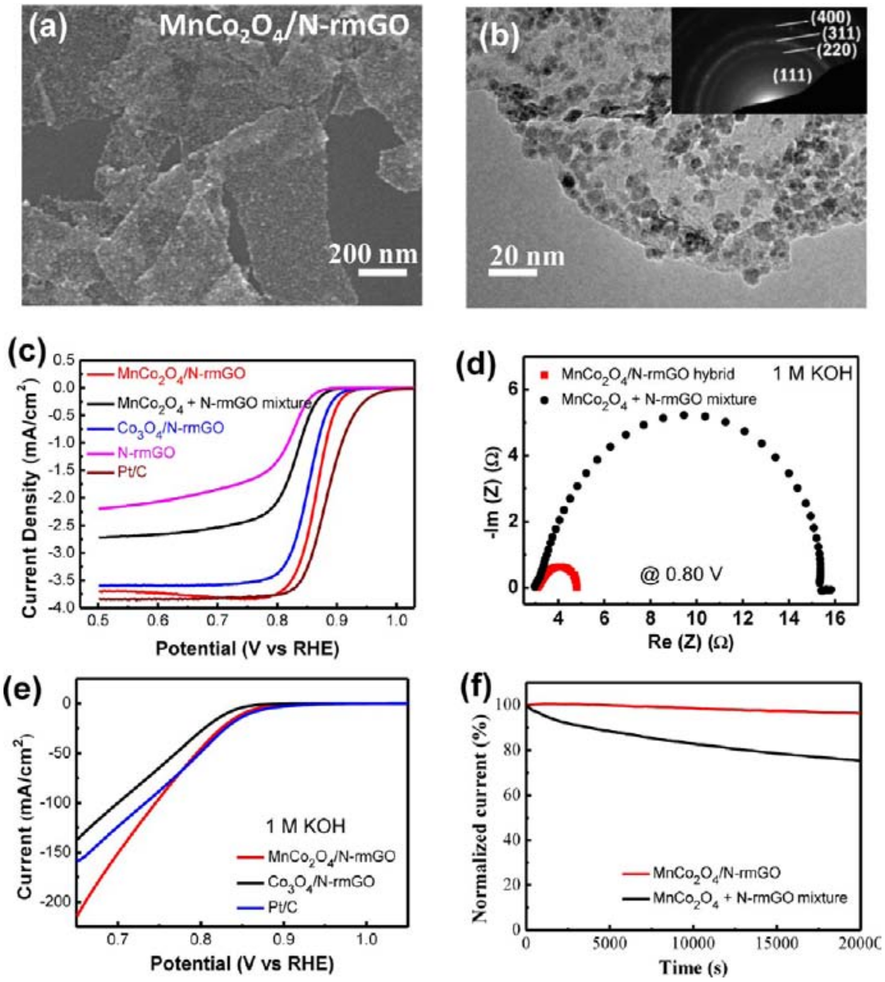

**Figure 11.** (a) SEM and (b) low magnification TEM images of the $MnCo_2O_4$/N-rmGO hybrid. Inset in (b) shows the electron diffraction pattern of the $MnCo_2O_4$/N-rmGO hybrid. (c) RDE voltammograms of the $MnCo_2O_4$/N-rmGO hybrid, $MnCo_2O_4$ + N-rmGO mixture, $Co_3O_4$/N-rmGO hybrid, N-rmGO, and Pt/C in $O_2$-saturated 1 M KOH at a sweep rate of 5 mV/s at 1600 rpm. (d) Impedance spectra of the $MnCo_2O_4$/N-rmGO hybrid and the mixture of $MnCo_2O_4$ and N-rmGO at 0.8 V vs RHE. (e) Oxygen reduction polarization curves of the $MnCo_2O_4$/N-rmGO hybrid, $Co_3O_4$/N-rmGO hybrid, and Pt/C on carbon fiber papers in 1 M KOH electrolyte. (f) Chronoamperometric responses of the $MnCo_2O_4$/N-rmGO hybrid and $MnCo_2O_4$ + N-rmGO mixture on carbon fiber paper electrodes kept at 0.70 V vs RHE in $O_2$-saturated 1 M KOH. Catalyst loading is ~0.24 mg/cm$^2$ for all samples. Reproduced with permission from ref 33e. Copyright 2012 American Chemical Society.

slightly lower activity than a commercial Pt/C catalyst (Etek 20% Pt on Vulcan XC-72) (Figure 10e) but much better stability (Figure 10f) at various alkaline media. High activity and stability of $Co_3O_4$/N-rmGO for ORR are the major features of the hybrid electrocatalyst.

Although the $Co_3O_4$/N-rmGO hybrid afforded higher ORR current density than the $Co_3O_4$/rmGO hybrid (Figure 10e), both hybrids exhibited similar ORR onset potentials (Figure 10c), suggesting that the active sites for ORR were similar in both hybrids but that the ORR activity could be enhanced by N doping of mGO. Systematic decrease in the ORR activity was observed when lowering the Co loading on graphene from 20% to 3% in the $Co_3O_4$/N-rmGO hybrid catalyst.[33b] The physical mixtures of $Co_3O_4$ with rmGO or N-rmGO were found to afford lower ORR activity and stability than the corresponding hybrid material. These results suggested that Co oxide species are the active sites for ORR and strong coupling with graphene especially N-doped graphene could lead to an ORR catalyst with high activity and stability.

$Co_3O_4$/NGO hybrids made from GO with different oxidation degrees were synthesized, and their catalytic performances were compared. The hybrid made from mGO outperformed those made from either less oxidized GO or heavily oxidized Hummers' GO.[33b] A similar trend was also observed in CNT hybrids.[33g] The results indicated that a balanced degree of oxidation to afford sufficient functional groups on carbon materials and electrical conductivity was important to the high activity of the resulting hybrid materials.

**5.2. $MnCo_2O_4$/N-Doped Graphene for ORR Electrocatalysis.** To further enhance the hybrid catalyst, we developed manganese-cobalt spinel/graphene hybrids, since cation substitution by Mn, Ni, or Cu into $Co_3O_4$ has shown higher electrocatalytic activity for ORR than pure $Co_3O_4$.[40,59] The hybrids were synthesized by a similar method as for the $Co_3O_4$/N-rmGO hybrid using $Co(OAc)_2$ and $Mn(OAc)_2$ at a certain ratio in the first-step solution-phase synthesis.[33e] By controlling the reactant ratio of $Co(OAc)_2$/$Mn(OAc)_2$ in 2/1, we grew $MnCo_2O_4$ nanocrystals in cubic spinel phase on graphene sheets to form strongly coupled $MnCo_2O_4$/N-rmGO hybrid (Figure 11a,b). Rotating disk electrode (RDE) measurements revealed that the $MnCo_2O_4$/N-rmGO hybrid catalyst outperformed N-rmGO and the free $MnCo_2O_4$ nanoparticle

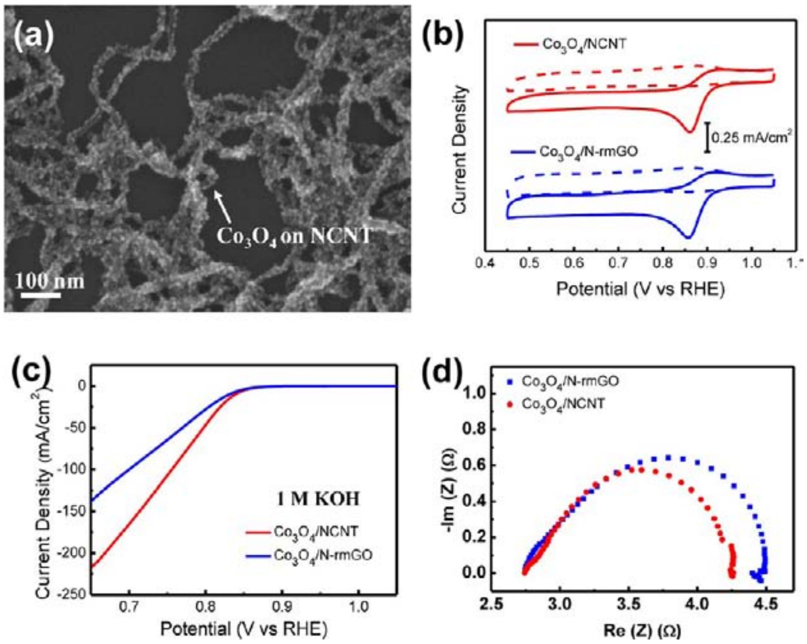

**Figure 12.** (a) SEM images of the $Co_3O_4$/NCNT hybrid. (b) CV curves of the $Co_3O_4$/NCNT and $Co_3O_4$/N-rmGO hybrids on glassy carbon electrodes in $O_2$-saturated (solid line) or $N_2$-saturated (dash line) 1 M KOH. Catalyst loading was 0.10 mg/cm$^2$ for both samples. (c) Oxygen reduction polarization curves of the $Co_3O_4$/NCNT and $Co_3O_4$/N-rmGO hybrids loaded on carbon fiber paper in 1 M KOH electrolyte. (d) Impedance spectra of $Co_3O_4$/NCNT and $Co_3O_4$/N-rmGO hybrids at 0.8 V vs RHE in 1 M KOH. Catalyst loading is ~0.24 mg/cm$^2$ for all samples in (c) and (d). Reproduced with permission from ref 33g. Copyright 2012 American Chemical Society.

mixture with N-rmGO sheets in terms of disk current density and half-wave potential (Figure 11c). In electrochemical impedance spectroscopy measurements, the $MnCo_2O_4$/N-rmGO hybrid showed a much smaller semicircle than the mixture and free $MnCo_2O_4$ nanoparticles at the ORR operation potential of 0.8 V, indicating a much smaller charge-transfer resistance for the hybrid materials during ORR (Figure 11d).[60] These results suggested that the high catalytic activity of the $MnCo_2O_4$/N-rmGO hybrid resulted from the strong electrical coupling between $MnCo_2O_4$ nanoparticles and N-doped graphene sheets.

The $MnCo_2O_4$/N-rmGO hybrid outperformed the $Co_3O_4$/N-rmGO hybrid with a 20 mV more positive half-wave potential (Figure 11c). Consistent with the RDE measurement, the $MnCo_2O_4$/N-rmGO hybrid showed higher current density than pure $Co_3O_4$/N-rmGO hybrid (Figure 11e) from polarization curves measured on TCFP. The current density of $MnCo_2O_4$/N-rmGO hybrid even exceeded that of Pt/C at potentials <0.75 V (Figure 11e). Both the $MnCo_2O_4$/N-rmGO and $Co_3O_4$/N-rmGO hybrids exhibited similar surface area. The enhanced electrocatalytic activity was attributed to Mn substitution.[33e] This result also suggested that the spinel oxide nanocrystals on the graphene sheets were the active sites in the hybrid materials.

The $MnCo_2O_4$/N-rmGO hybrid also exhibited excellent stability for ORR through chronoamperometric measurements (Figure 11f), much more stable than the mixture of nanoparticles and N-rmGO. The ORR current density at a constant voltage of 0.70 V decreased by only 3.5% for the hybrid catalyst over continuous operation in 5.5 h, while the physical mixture sample exhibited ~25% decreases in the same operation. This suggested that the coupling between nanoparticles and GO remains intact in the hybrid case in the ORR potential range.

### 5.3. Graphene vs Carbon Nanotubes for Making Inorganic/Nanocarbon Hybrids.

Through our work, we found that inorganic/graphene hybrids required a suitable oxidation degree of GO to afford high performance of electrocatalysis. GO with a suitable degree of oxidation should be used for high-performance catalysts, since functional groups are needed for nucleating and anchoring nanocrystals on GO sheets to achieve strong attachment. However, a dilemma is that the existence of defects and functional groups on graphene sheets could lower its electroconductivity and limit the catalytic performance of the hybrid material. For example, $Co_3O_4$/N-doped graphene hybrid prepared by the original Hummers GO method afforded much lower performance than the $Co_3O_4$/N-rmGO hybrid prepared with mGO.[33b] Harsh oxidation of GO caused a problem due to the imbalance of the inorganic-carbon coupling interactions and the electrical conductivity of the hybrid material.

Recently, we realized that multiwalled CNT (MWCNT) or few-walled CNTs could overcome this problem as the inner graphitic walls could remain intact to provide highly conducting network, while the outermost wall can be oxidized and functionalized to afford chemical reactivity. This was proven to be the case in the work of developing a nanotube–graphene complex for ORR in acidic conditions.[33d] Therefore, it is interesting to hybridize CNTs with active nonprecious inorganic nanocrystals, such as $Co_3O_4$, to afford high-performance ORR catalysts, which has not been done previously.

We synthesized a $Co_3O_4$/NCNT (N-doped CNT) hybrid by growing $Co_3O_4$ nanocrystals on oxidized MWCNT using the same method as for the $Co_3O_4$/N-rmGO hybrid (Figure 12a).[33g] The oxidized MWCNT was prepared by the modified Hummers method with $KMnO_4/C = 1/1$ in mass ratio, higher than that to prepare mGO (1/2).[33b,g] CV spectra showed that both the $Co_3O_4$/NCNT and $Co_3O_4$/N-rmGO hybrids

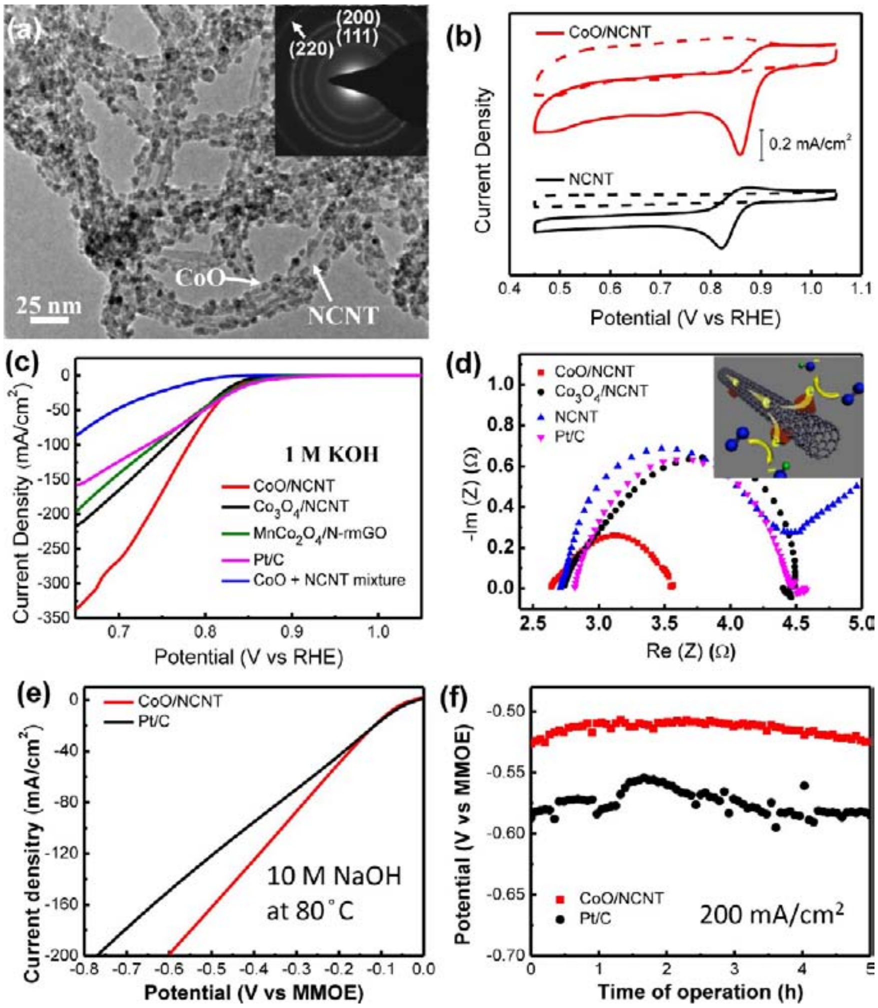

**Figure 13.** (a) TEM image of the CoO/NCNT hybrid with inset showing the electron diffraction pattern of the hybrid. (b) CV curves of CoO/NCNT hybrid and NCNT on glassy carbon electrodes in $O_2$-saturated (solid line) or $N_2$-saturated (dash line) 1 M KOH. Loading was 0.10 mg/cm$^2$ for both samples. (c) Oxygen reduction polarization curves of the CoO/NCNT hybrid, $Co_3O_4$/NCNT hybrid, $MnCo_2O_4$/N-rmGO hybrid, Pt/C, and CoO plus NCNT mixture loaded on carbon fiber paper in 1 M KOH electrolyte. (d) Impedance data of CoO/NCNT, Co3O4/NCNT hybrids, NCNT, and Pt/C at 0.8 V vs RHE. Inset in (d) shows a cartoon of CoO/NCNT hybrid for oxygen reduction catalysis. Catalyst loading was ~0.24 mg/cm$^2$ for all samples in (c) and (d). (e,f) Catalytic performance of the CoO/NCNT hybrid and Pt/C in 10 M NaOH at 80 C. (e) Oxygen reduction polarization curves without *iR* compensation of the CoO/NCNT hybrid and Pt/C. (f) Potential vs time response of the oxygen cathode catalyzed by the CoO/NCNT hybrid and Pt/C at 200 mA/cm$^2$. Catalyst loading is ~0.48 mg/cm$^2$ for all samples in (e) and (f). Reproduced with permission from ref 33g. Copyright 2012 American Chemical Society.

exhibited the same onset and peak potentials for ORR, suggesting similar active sites in both hybrids (Figure 12b). The $Co_3O_4$/N-rmGO hybrid showed a larger loop compared to the $Co_3O_4$/NCNT hybrid in the CV data measured under $N_2$, indicating higher electrochemically active surface area in the N-rmGO hybrid. This was consistent with the BET results that BET surface area of $Co_3O_4$/N-rmGO was ~210 m$^2$/g, while $Co_3O_4$/NCNT was ~154 m$^2$/g. However, when loaded onto TCFP for measurements, the $Co_3O_4$/NCNT hybrid showed significantly higher ORR current density than the $Co_3O_4$/N-rmGO hybrid (Figure 12c). The Nyquist plots of electrochemical impedance data indicated that the $Co_3O_4$/NCNT hybrid exhibited a smaller charge-transfer resistance for ORR with a smaller semicircle for the $Co_3O_4$/NCNT hybrid than the N-rmGO hybrid at the ORR operation potential of 0.8 V (Figure 12d). Direct electrical resistance measurement on the sample pellet showed that the $Co_3O_4$/NCNT hybrid had a smaller resistance (~40−60 Ω) than the $Co_3O_4$/N-rmGO hybrid (~200−300 Ω). These results suggested that higher electrical conductivity in the NCNT hybrid could account for improved ORR performance in the $Co_3O_4$/NCNT hybrid.

In a related work, we employed oxidized MWCNTs as substrates for nucleating and growing $Ni(OH)_2$ nanoplates and observed higher specific capacitance values of the $Ni(OH)_2$ nanoplates grown on MWCNTs than the nanoplates grown on graphene sheets.[47a] Thus far, our results suggest that oxidized multiwalled or few-walled CNTs are advantageous over GO for the formation of inorganic/nanocarbon hybrid when the inorganic nanomaterials are extremely insulating electrically. In this case, strong coupling of the nanoparticles to a nanocarbon material (e.g., CNT) with high electrical conductivity is of particular importance to the electrochemical characteristics of the resulting hybrid. GO on the other hand is advantageous in providing higher surface area for constructing hybrid materials. GO sheets also possess the ability to host materials with various shapes include nanorods and plates and are highly effective in hybridizing with inorganic nanoparticles

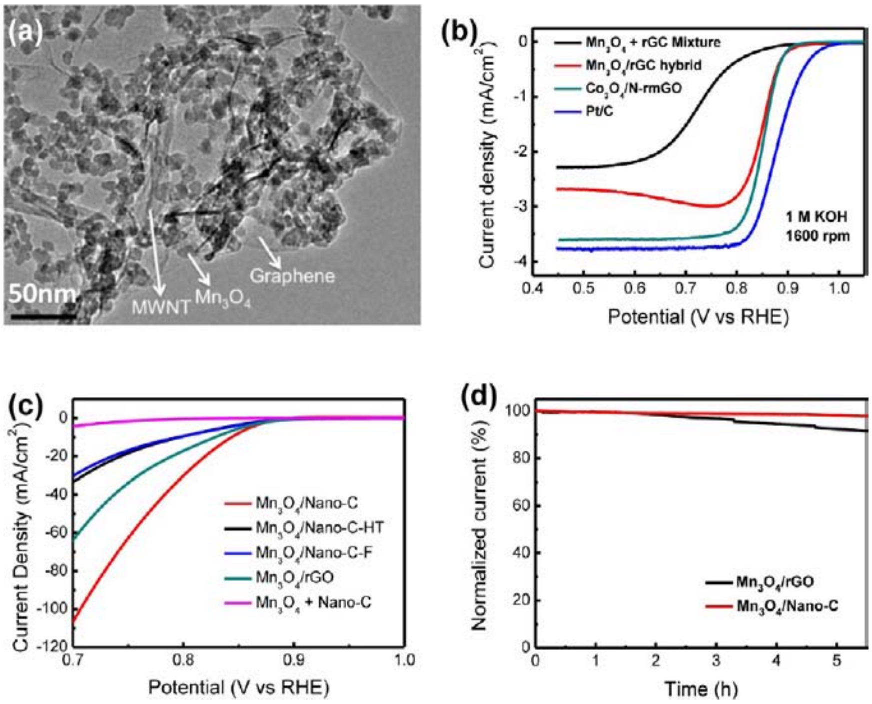

**Figure 14.** (a) TEM image of the $Mn_3O_4$/Nano-C hybrid. (b) RDE voltammograms of the $Mn_3O_4$/Nano-C hybrid, $Mn_3O_4$ + Nano-C mixture, the $Co_3O_4$/N-rmGO hybrid, and Pt/C in $O_2$-saturated 1 M KOH at a sweep rate of 5 mV/s at 1600 rpm. The baseline in $N_2$-saturated electrolyte was subtracted. Catalyst loading was 0.1 mg/cm$^2$. (c) Oxygen reduction polarization curves of the $Mn_3O_4$/Nano-C hybrid, $Mn_3O_4$ + Nano-C mixture, $Mn_3O_4$/Nano-C first-step product ($Mn_3O_4$/Nano-C-F), $Mn_3O_4$/NC hydrothermal sample ($Mn_3O_4$/Nano-C-HT), and $Mn_3O_4$/rGO hybrid loaded on carbon fiber papers in $O_2$-saturated 1 M KOH at a scan rate of 5 mV/s. (d) Chronoamperometric responses of $Mn_3O_4$/Nano-C and $Mn_3O_4$/rGO on carbon fiber paper electrodes kept at 0.70 V vs RHE in $O_2$-saturated 1 M KOH. Catalyst loading was ~0.24 mg/cm$^2$. Reproduced with permission from ref 33f. Copyright 2012 Springer.

with relatively high intrinsic electrical conductivity to afford advanced electrochemical materials.

### 5.4. Gas-Phase Annealing vs Hydrothermal Reactions.

We carried out gas-phase annealing to replace hydrothermal reaction as the second step and synthesized a cobalt oxide/CNT hybrid.[33g] The first-step product was thermal annealed at 400 °C in a $NH_3$/Ar atmosphere, yielding cobalt oxide nanocrystals growing on NCNT in cubic CoO structure (Figure 13a). CV data suggested that the CoO/NCNT hybrid had higher ORR electrocatalytic activity than NCNT control prepared by the same method but similar to the $Co_3O_4$/NCNT hybrid in terms of ORR onset and peak potential (Figure 13b). This also suggested that both CoO/NCNT and $Co_3O_4$/NCNT hybrids possessed similar active site in nature, which was reasonable as the surface of CoO nanoparticle was easily oxidized to $Co_3O_4$.[33g]

When measured on TCFP, the CoO/NCNT hybrid synthesized by the gas-phase annealing method exhibited the highest ORR performance to date among our various hybrid materials. The CoO/NCNT afforded significantly higher ORR current density than the $Co_3O_4$/NCNT hybrid, the commercial Pt/C catalyst and the $MnCo_2O_4$/N-rmGO hybrid at moderate overpotentials (<0.80 V vs RHE) (Figure 13c). The CoO/NCNT catalyst also exhibited the smallest semicircle in the Nyquist plot compared to Pt/C, $Co_3O_4$/NCNT, and NCNT (Figure 13d), suggesting the lowest charge-transfer resistance from the electrode to oxygen molecule during ORR. Gas-phase annealing in $NH_3$ led to better reduction of oxCNTs, lowing the resistance of the hybrid compared to hydrothermally derived $Co_3O_4$/NCNT hybrid. By the same token, we found that $NH_3$ annealing of the $Co_3O_4$/N-rmGO hybrid[33b] yielded a CoO/N-rmGO hybrid also affording higher ORR current density than the hydrothermally synthesized $Co_3O_4$/N-rmGO hybrid.[33g] These results suggested that gas-phase annealing of hybrid materials was effective in improving the ORR performance of the hybrid material due to the better reduction at high temperatures especially in the presence of $NH_3$.

Recently, we evaluated the ORR catalytic performance of the CoO/NCNT hybrid in 10 M NaOH at 80 °C, a condition used for oxygen depolarized cathode in chlor-alkali electrolysis.[55] We found that the CoO/NCNT hybrid afforded higher ORR current than Pt/C at potential voltages < −0.15 V vs the Hg/HgO reference electrode (MMOE) (Figure 13e), with little change in the cathode potential when operated chronoamperometrically at 400 mA/mg for 5 h (Figure 13f). The high ORR activity and excellent durability of the CoO/NCNT catalyst in such harsh conditions are important features of this material, making it a promising electrocatalyst for high-energy reaction processes involving chlor-alkali electrolysis.

### 5.5. Manganese Oxide/Nanocarbon Hybrid.

Owing to high abundance, low cost, and environmental benignity as well as rich electrochemical properties, manganese oxides have the potential to be sustainable and efficient electrocatalysts for ORR. However, most of the current electrocatalysts based on manganese oxides suffered from low activity and rapid activity decay.[32,61] Our success on cobalt oxide hybrid systems motivated us to explore high-performance manganese oxide ORR catalyst based on hybrids with nanocarbon materials.[33f]

Manganese oxide hybrid was prepared by a modified two-step method to afford direct growth of $Mn_3O_4$ nanoparticles on nanocarbon substrate (Nano-C) containing a mixture of GO and oxidized MWCNT with a mass ratio of 10/1 (Figure

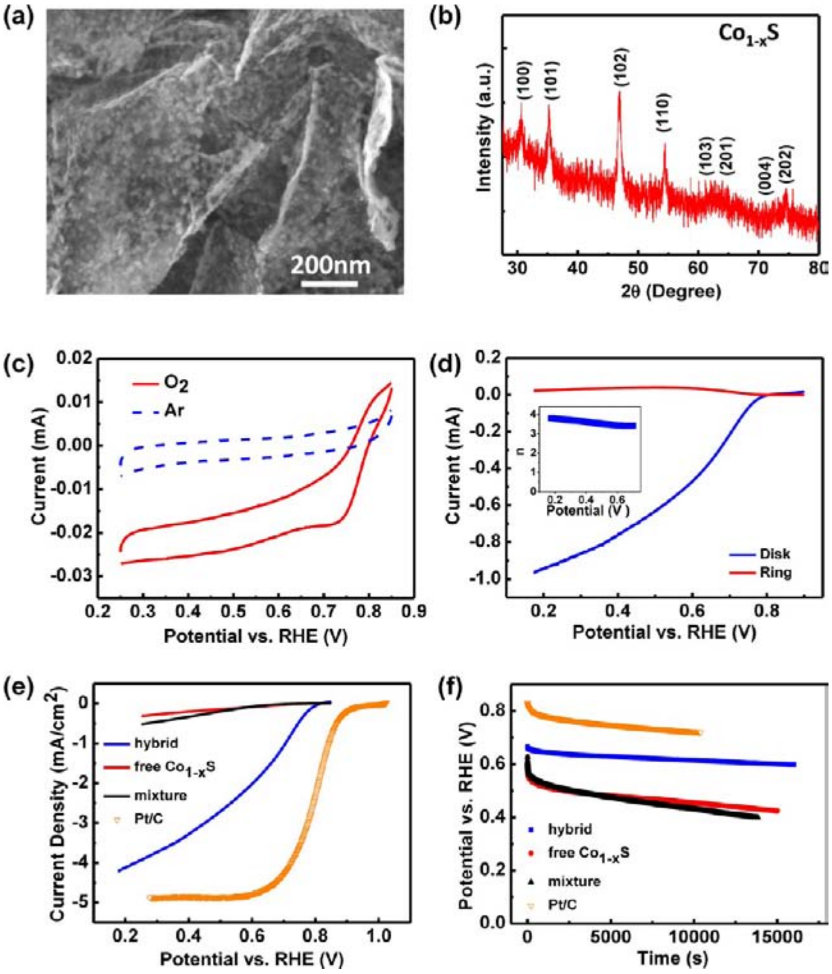

**Figure 15.** (a) SEM image of the $Co_{1-x}S$/rGO hybrid. (b) XRD spectrum of a compacted film of the $Co_{1-x}S$/rGO. (c) CV curves of the $Co_{1-x}S$/rGO hybrid on glassy carbon electrodes in $O_2$-saturated (red line) and Ar-saturated (blue line) 0.5 M $H_2SO_4$ with a sweep rate of 10 mV/s. Catalyst loading was 0.285 mg/cm$^2$. (d) RRDE curves of the $Co_{1-x}S$/rGO (loading ~0.1 mg/cm$^2$) in $O_2$-saturated 0.5 M $H_2SO_4$ with a sweep rate of 5 mV/s at a rotating speed of 1600 rpm. Inset showed the electron-transfer number $n$ at different potentials calculated from RRDE curves. (e)RDE curves of the $Co_{1-x}S$/rGO hybrid, free $Co_{1-x}S$ nanoparticles, physical mixture of rGO and $Co_{1-x}S$ nanoparticles, and Pt/C at a rotating speed of 1600 rpm in $O_2$-saturated 0.5 M $H_2SO_4$ with a sweep rate of 5 mV/s. Catalyst loading was 0.1 mg/cm$^2$ for all the samples. (f) Galvanostatic constant current discharge curves of the $Co_{1-x}S$/rGO hybrid, free $Co_{1-x}S$ nanoparticles, physical mixture of rGO and $Co_{1-x}S$ nanoparticles, and Pt/C at a rotating speed of 1600 rpm in $O_2$-saturated 0.5 M $H_2SO_4$. Discharge current density was ~1.5 mA/cm$^2$ for $Co_{1-x}S$/rGO hybrid, ~0.05 mA/cm$^2$ for free $Co_{1-x}S$ nanoparticles and physical mixture of rGO and $Co_{1-x}S$ nanoparticles, and ~1.5 mA/cm$^2$ for Pt/C. Reproduced with permission from ref 33c. Copyright 2011 Wiley-VCH.

14a).[33f] Due to the high surface area of GO, most of the manganese oxide nanoparticles were grown on graphene sheets in the $Mn_3O_4$/Nano-C hybrid, while the oxidized MWCNTs addition was intended to improve the electrical conductivity of the hybrid considering the highly insulating nature of $Mn_3O_4$.

RDE measurements revealed that the ORR electrocatalytic activity of the $Mn_3O_4$/Nano-C hybrid was higher than the physical mixture of free $Mn_3O_4$ nanoparticles and Nano-C[33f] and comparable to the $Co_3O_4$/N-rmGO hybrid[33b] (Figure 14b). In terms of both half-wave potential and disk current, the $Mn_3O_4$/Nano-C hybrid was among one of the highest activity manganese oxide-based ORR catalysts operating in alkaline conditions. Consistent with RDE result, measurement on TCFP showed that the $Mn_3O_4$/Nano-C hybrid afforded much higher ORR current density than the physical mixture (Figure 14c). Air calcination in the second step was found to be important to the high activity (Figure 14c), attributed to higher density of Mn (III) species on the surface of manganese oxide nanoparticles responsible for active sites of ORR. Stability of the $Mn_3O_4$/Nano-C catalyst was also excellent (Figure 13d).[33f] These results confirmed that hybridization of metal oxide nanoparticles including cobalt oxide and manganese with nanocarbon materials through oxygen functional groups represented a viable approach to high-performance electrocatalysts. We also found that rationally selecting graphene, CNT, or their combinations with suitable oxidation degrees is important to produce the highest performance electrocatalyst based on nonprecious metal inorganic materials.

## 6. ORR ELECTROCATALYST IN ACIDIC MEDIA

Proton exchange membrane (PEM) based fuel cell system is currently the leading fuel cell technology as it affords high power density and minimal material problems compared to other systems, making it more suitable for the applications in transportation and portable power.[62] A key limitation for the development of PEM fuel cell lies in the cathode ORR electrocatalyst, which operates in acidic conditions with high efficiency, good durability, and low cost.[63] Nonprecious metal-based electrocatalysts, such as metal–nitrogen complexes on carbon matrixes and metal chalcogenides could offer low-cost alternatives for the precious metal catalysts, although their activity and stability are still lower than the precious metal counterparts.[64] Nanocarbon hybrids could open up new strategies to improve these catalysts to attain higher activity and stability for ORR in acidic solutions.

**6.1. Cobalt Sulfide-Graphene Hybrid.** Cobalt sulfides are among the most active ORR electrocatalysts based on nonprecious metal chalcogenides in acidic meida.[65] However, their ORR catalytic activities are far below Pt, and the reduction pathway is dominant by 2*e* processes.[65c] For improved cobalt sulfide-based electrocatalyst, we synthesized a cobalt sulfide-graphene hybrid by selective growth of $Co_{1-x}S$ nanoparticles on rGO through a two-step method.[33c] A low-temperature solution-phase reaction by reacting $Co(Ac)_2$ with thioacetamide (TAA) at 80 °C was conducted in the first step, followed by gas-phase annealing step at 500 °C in Ar atmosphere, affording $Co_{1-x}S$ nanoparticles on rGO sheets. The cobalt sulfide nanoparticles were selectively grown on graphene sheets with an average particle size of ~10–20 nm (Figure 15a) in the hexagonal $Co_{1-x}S$ phase as revealed by XRD (Figure 15b).

CV measurements showed that the ORR onset and peak potential for the $Co_{1-x}S$/rGO hybrid were located at ~0.8 and ~0.73 V vs RHE, respectively, in 0.5 M $H_2SO_4$ at 25 °C (Figure 15c). The electron-transfer number of the hybrid determined by RRDE measurement was ~3.4 at 0.7 V and inceased steadily to ~3.8 at 0.18 V (Figure 15d). At 0.7 V in the RDE measurments, our $Co_{1-x}S$/rGO hybrid catalyst afforded a current density of ~1.1 mA/cm$^2$, higher than previous reports for cobalt chalcogenide-based catalysts. Physical mixture of free $Co_{1-x}S$ nanoparticles and rGO sheets exhibited similar onset potential as the $Co_{1-x}S$/rGO hybrid, indicating that the active sites in these catalysts were oringinated from $Co_{1-x}S$ (Figure 15e). Direct growth on rGO for the $Co_{1-x}S$/rGO hybrid afforded the most effective way to render $Co_{1-x}S$ nanoparticles electrochemically active, affording high ORR activity for this material. The $Co_{1-x}S$/rGO hybrid also showed improved the electrocatalytic stability than the free $Co_{1-x}S$ particles mixed with rGO (Figure 15f).

We also synthesized a $Co_{1-x}S$/MWCNT hybrid by the same two-step method (Figure 16a).[66] In the measurement on TCFP in 0.5 M $H_2SO_4$, the $Co_{1-x}S$/MWCNT hybrid exhibited further improved ORR performance than the $Co_{1-x}S$/rGO hybrid. At a potential of 0.50 V, the $Co_{1-x}S$/MWCNT showed an ORR current density of 76.5 mA/cm$^2$, significantly higher than that of the $Co_{1-x}S$/rGO hybrid electrode (30.8 mA/cm$^2$) (Figure 16b). Electrochemical impedance spectroscopy revealed that the $Co_{1-x}S$/MWCNT hybrid showed a smaller charge-transfer resistance than the $Co_{1-x}S$/rGO hybrid (~4.5 Ω vs ~8.7 Ω), consistent with the higher ORR current density afforded by the $Co_{1-x}S$/MWCNT hybrid material. This again suggested inorganic hybrids with mildly oxidized MWCNT could outperform GO counterparts owing to higher electrical conductivity of the hybrid materials, leading to enhanced electrochemical properties.

**6.2. Carbon Nanotube–Graphene Complexes.** Recent advances[9a,67] have shown that metal-N/C electrocatalysts made by pyrolyzing metal and nitrogen containing precursors on solid carbon supports are promising low-cost alternatives to Pt-based electrocatalysts for ORR in acidic conditions. However, the insufficient activity and low stability require further improvement for practical applications.[68] Carbon nanotube-based electrocatalysts have been explored due to their high electrical conductivity and corrosion resistance. Unfortunately, most of CNT-based ORR catalysts showed low activities in acidic media, possibly due to low density of catalytic sites formed on the less defective CNTs.

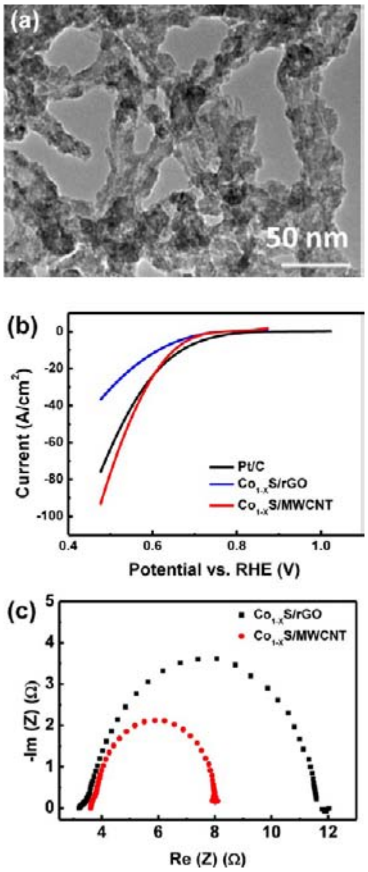

**Figure 16.** (a) TEM image of the $Co_{1-x}S$/MWCNT hybrid. (b) Linear sweep voltammetry curves of the $Co_{1-x}S$/MWCNT hybrid, the $Co_{1-x}S$/rGO hybrid and Pt/C catalyst loaded on TCFP measured $O_2$-saturated 0.5 M $H_2SO_4$ with a sweep rate of 5 mV/s. Catalyst loading was 0.24 mg/cm$^2$. (c) AC impedance spectra of the $Co_{1-x}S$/MWCNT and $Co_{1-x}S$/rGO hybrids measured at 0.60 V in 0.5 M $H_2SO_4$.

We decided to extend our preparation of GO sheets to the oxidation of few-walled CNTs (FWCNTs, mostly double-walled) as a way to introduce abundant structural defects on the outer walls of FWCNTs for hosting M-N$_x$ ORR active sites (Figure 17a).[33d] FWCNTs were first oxidized under a condition harsher than the typical Hummers method, affording partial unzipping of the outer walls into nanoscale graphene pieces attached to the mostly intact inner walls. Upon subsequent annealing in ammonia gas, the abundant edges and defect sites on nanographene reacted with iron impurities (inherited from catalyst seeds for FWCNT growth) and ammonia, giving an efficient ORR catalyst comprised of CNT–nanographene complexes (NT-G)(Figure 17a,b).

The NT-G catalyst displayed good electrocatalytic activity and durability for ORR in acidic media. In 0.1 M $HClO_4$, the catalyst afforded an ORR onset potential of ~0.89 V and a half-wave potential of ~0.76 V vs RHE in RRDE polarization curves (Figure 17c), which was ~80 mV away from the 20 wt % Pt/C benchmark. The NT-G was more active than other CNT-based electrocatalysts in acidic conditions[69] with a more positive onset potential by >150 mV and well-defined plateaus of

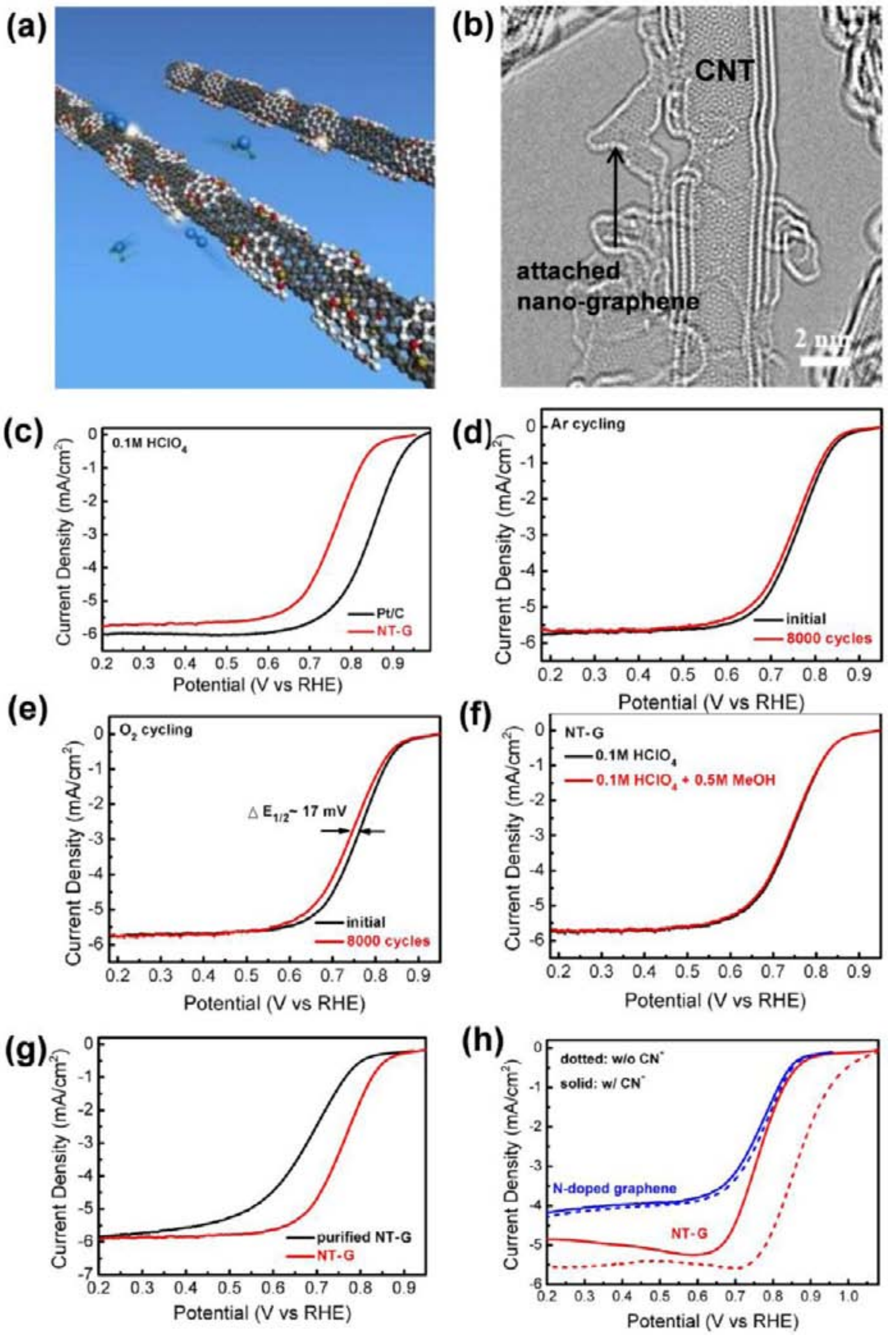

**Figure 17.** (a) Schemetic representations of ORR catalized by NT-G. (b) TEM images of the NT-G material showing damaged outer walls and exfoliated graphene pieces attached to double- or triple-walled CNT. (c) RDE polarization curves of Pt/C (black) and NT-NG (red) in $O_2$-saturated 0.1 M $HClO_4$. The loading of catalysts is 16 $\mu g_{Pt}/cm^2$ for Pt/C and 0.485 $mg/cm^2$ for NT-NG. Electrode rotation speed is 1600 rpm. Scan rate is 5 mV/s. Pt data are collected from anodic sweeps. (d,e) RDE polarization curves of the NT-NG catalyst before and after 8000 potential cycles in Ar (d) and $O_2$ (e) saturated 0.1 M $HClO_4$, respectively. The potential cycling is carried out between 0.6 and 1.0 V vs RHE at 50 mV/s. (e) RDE polarization curves of NT-NG in $O_2$ saturated 0.1 M $HClO_4$ with (red) or without (black) 0.5 M methanol. (f) RRDE polarization curves of NT-G respectively in $O_2$ saturated 0.1 M $HClO_4$ with (red) or without (black) 0.5 M methanol. (g) RDE polarization curve of purified NT-G in comparison with NT-NG without intentional Fe impurity removal in $O_2$-saturated 0.1 M $HClO_4$. (h) RDE polarization curves of NT-G (red) and N-doped graphene (blue) in $O_2$-saturated 0.1 M KOH with (solid lines) or without (dotted lines) 10 mM $CN^-$. Reproduced with permission from ref 33d. Copyright 2012 Nature Publishing Group.

diffusion limiting currents. Its mass activity derived from the RRDE disk current was 4.4 A/g at 0.80 V, among the most active nonprecious metal-based ORR catalysts in acid conditions.[68,70] RRDE measurements revealed that the NT-G catalyzed ORR was through a mainly 4*e* pathway with a low $H_2O_2$ yield < 4% at all operating potentials.

In addition to its high activity, the NT-G catalyst also exhibited good cycling durability in acidic conditions as assessed by DOE's accelerated durability test protocol. After 8000 continuous cycles between 0.6 and 1.0 V at 50 mV/s in 0.1 M $HClO_4$, the half wave potential of NT-G showed a small negative shift of ~11 mV under Ar cycling (Figure 17d) and

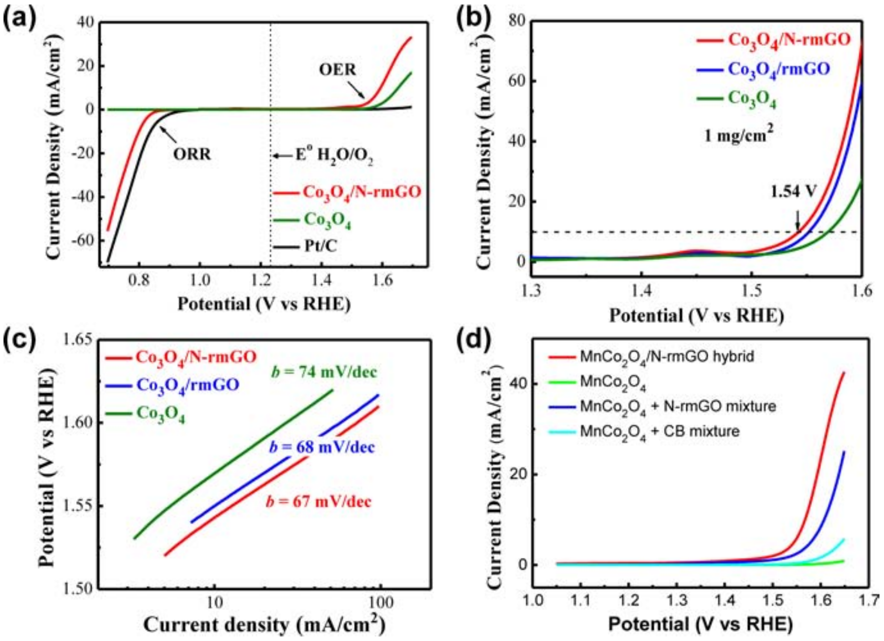

**Figure 18.** (a) Oxygen electrode activities within the ORR and OER potential window of the $Co_3O_4$/N-rmGO hybrid, $Co_3O_4$ nanocrystal, and Pt/C catalysts dispersed on carbon fiber paper in $O_2$-saturated 0.1 M KOH. (b) Polarized currents in the OER region of Ni foam electrodes loaded with the $Co_3O_4$/N-rmGO hybrid, $Co_3O_4$/rmGO hybrid, and $Co_3O_4$ nanocrystals (a high catalyst loading of ~1 mg/cm$^2$) measured in 1 M KOH. (c) Tafel plots of OER currents in (b). Reproduced with permission from ref 33b. Copyright 2011 Nature Publishing Group. (d) Oxygen evolution currents of the $MnCo_2O_4$/N-rmGO hybrid, $MnCo_2O_4$ nanoparticles, $MnCo_2O_4$ + N-rmGO mixture, and $MnCo_2O_4$ + CB mixture dispersed on carbon fiber paper in 1 M KOH electrolyte. Catalyst loading is ~0.24 mg/cm$^2$ for all samples. Reproduced with permission from ref 33e. Copyright 2012 American Chemical Society.

~17 mV under $O_2$ cycling (Figure 17e), while Pt/C catalyst measured in the same condition exhibited >20 mV negative shift under $O_2$ cycling. Furthermore, the NT-G catalyst showed little activity loss when exposed to methanol, in contrast to the methanol poisoning effect on Pt/C catalyst (Figure 17f).

We found that iron and nitrogen played important roles in forming the active NT-G catalyst. We prepared purified FWCNTs by removing most metal impurity to afford a material with a much lower Fe content (~0.11 wt.% vs ~1.1% in NT-G). The purified NT-G material exhibited a ~100 mV more negative onset potential and half-wave potential than the NT-G catalyst without intentional Fe removal (Figure 17g). Moreover, we observed that in the presence of low-concentration KCN, the ORR activity of Fe-containing NT-G was significantly suppressed in alkaline media, suggesting coordination of cyanide to Fe and thus blocking the active sites. We observed that Fe-free nitrogen-doped graphene showed no such deactivation by cyanide (Figure 17h). These results suggested that Fe was a key element involved in the ORR active sites in our NT-G catalyst, similar to the roles played by nitrogen. A NT-G material annealed in Ar or vacuum without the presence of $NH_3$ exhibited much lower ORR activity, suggesting the important role of N-doping. This work also found that metal impurities in as-grown CNT materials could play important roles in downstream ORR catalysis reactions and should be carefully taken into consideration.[33d]

## 7. ELECTROCATALYST FOR OER

We found that in addition to ORR activity, our $Co_3O_4$/rmGO hybrid showed higher catalytic activity than free $Co_3O_4$ nanoparticles for OER, making it an efficient bifunctional catalyst for oxygen reduction and evolution (Figure 18a), similar to manganese oxide[19d] and spinel CoMnO[12b] catalysts. We performed a detailed study of the OER performance of the catalysts loaded into Ni foam at ~1 mg/cm$^2$ in 1 M KOH at room temperature (Figure 18b).[33b] Both the $Co_3O_4$/rmGO and $Co_3O_4$/N-rmGO hybrids showed higher OER current density than free $Co_3O_4$ nanoparticles. The overpotential to reach 10 mA/cm$^2$ and the Tafel slope (Figure 18c) afforded by the $Co_3O_4$/rmGO and $Co_3O_4$/N-rmGO hybrid were small and compare favorably with other $Co_3O_4$ nanoparticle OER catalysts.[71] Unlike the ORR case, N-doping of graphene did not lead to obvious improvement of OER performance for $Co_3O_4$/N-rmGO vs $Co_3O_4$/rmGO. The OER activity of the $MnCo_2O_4$/N-rmGO hybrid was much higher than the physical mixture of $MnCo_2O_4$ nanoparticles with N-rmGO or carbon black (CB) (Figure 18d).[33e] Therefore, the $MnCo_2O_4$/N-rmGO hybrid could also serve as an efficient bifunctional catalyst.

Motivated by the high ORR activity and good OER activity of the $MnCo_2O_4$/N-rmGO hybrid in aqueous solutions, we explored the material as a cathode catalyst for Li-$O_2$ battery using 1 M $LiClO_4$ in propylene carbonate (PC) as the electrolyte (Figure 19a).[72] Li-$O_2$ batteries are promising energy storage systems with high gravimetric energy density than lithium ion batteries.[73] However, Li-$O_2$ cells suffer from high overpotential and short cycle lives, partially due to the low performance of electrocatalyst for oxygen reduction during discharge and inefficient oxygen evolution by lithium oxide during charging at the cathode side.[69b,73,74]

We found that the ORR catalytic activity of the $MnCo_2O_4$/N-rmGO hybrid in aqueous solutions could be translated to the organic electrolyte, giving a high discharging potential of the Li-$O_2$ cell (Figure 19b). The $MnCo_2O_4$/N-rmGO hybrid was also more active in catalyzing the charging reaction than N-doped graphene (N-rmGO), CB, and a mixture of $MnCo_2O_4$

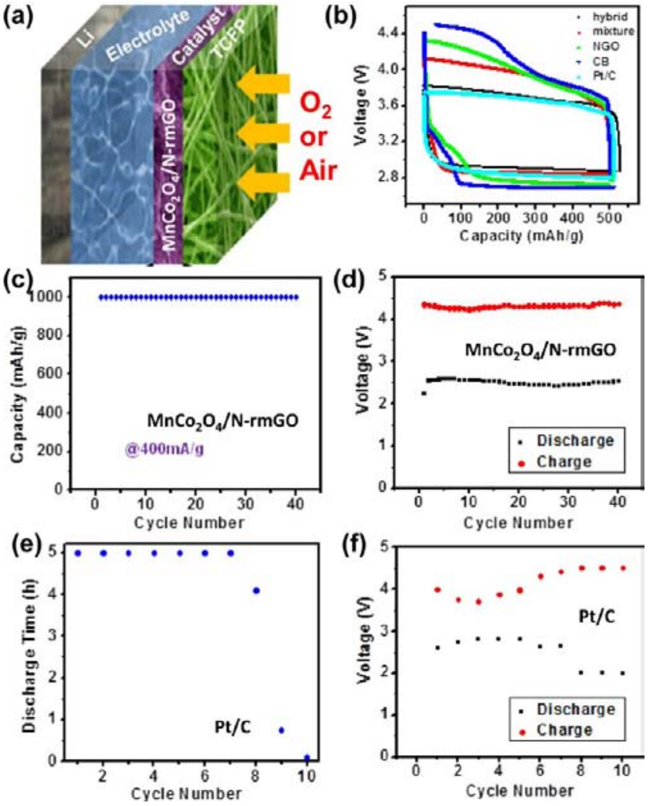

**Figure 19.** (a) Schematic structure of the Li-$O_2$ cell catalyzed by the $MnCo_2O_4$/N-rmGO hybrid. (b) Charging and discharging voltage profiles of Li-$O_2$ cells catalyzed by different catalysts at a current density of 100 mA/g. (c) Specific discharge capacity of the cell catalyzed by the $MnCo_2O_4$/N-rmGO hybrid over 40 cycles at 400 mA/g. (d) Cell voltage upon completion of each discharge (black) and charge (red) segment over the 40 cycles in (c). (e) Specific discharge capacity of the Li-$O_2$ cell catalyzed by Pt/C over 10 cycles. Current density was 100 mA/g for the first 6 cycles and 200 mA/g for the rest of cycles. (f) Cell voltage upon completion of each discharge (black) and charge (red) segment over the 10 cycles in (e). Reproduced with permission from ref 72. Copyright 2012 The Royal Society of Chemistry.

nanoparticles and CB (Figure 19b). The $MnCo_2O_4$/N-rmGO hybrid showed similar overpotential and charging−discharging performances as the benchmark Pt/C catalyst (Figure 19b). However, the hybrid catalyst exhibited much better cycling stability of the Li-$O_2$ cell than Pt/C through charge and discharge with a capacity cutoff of 1000 mAh/g over 40 cycles (Figure 19c), with little changes on the discharging and charging potentials (Figure 19d). Compared to the hybrid, the Pt/C catalyzed cell exhibited much faster increase in overpotential and shorter cycle life over cycling (Figure 19e,f)

The discharging and charging reactions on the cathode side of the Li-$O_2$ cells in organic electrolyte remain poorly understood. The charging reaction could involve the decomposition of carbonate electrolytes.[75] A possible consequence is that Pt/C, a poor OER catalyst in alkaline solutions, could catalyze the charging reaction of Li-$O_2$ cells with a similar overpotential as the OER active $MnCo_2O_4$/N-rmGO hybrid. Nevertheless, the substantial performance improvement afforded by the hybrid material over the physical mixture of $MnCo_2O_4$ and graphene suggested that the strong coupling within the hybrid structure played important roles in effectively and rapidly transfer charges to and from the catalytic active sites of the $MnCo_2O_4$ nanoparticles even in organic electrolytes.

## 8. $MOS_2$/GRAPHENE HYBRID ELECTROCATALYST FOR HER

$MoS_2$ is a promising nonprecious metal-based electrocatalyst for HER with moderate overpotential in the range of ∼0.1 to ∼0.4 V reported in the literature.[76] The HER active sites are suggested to arise from the sulfur edges,[77] but the reaction mechanism and pathways are still inconclusive. In an effort to improve the HER catalytic activity of $MoS_2$, we synthesized a $MoS_2$/rGO hybrid by solvothermal reaction of $(NH_4)_2MoS_4$ and mGO with hydrazine at 200 °C.[33a] This method produced $MoS_2$ nanoparticles selectively and uniformly grown on the graphene sheets (Figure 20a) in a form of 2D-like plates with thickness of 3−10 atomic layers and abundant edge structures (Figure 20b). In strong contrast, in the absence of GO, the exact same synthesis method produced $MoS_2$ coalesced into 3D-like particles of large sizes (Figure 20c),[33a] again highlighting the role of GO as a novel support material in directing the growth morphology of nanomaterials as discussed in Section 4.2.

We evaluated the HER activity of $MoS_2$/rGO hybrid catalyst on a glassy carbon electrode in 0.5 M $H_2SO_4$. Compared to $MoS_2$ nanoparticles and rGO alone or their physical mixture at the same loading, the $MoS_2$/rGO hybrid catalyst exhibited a smaller overpotential of ∼0.1 V and a much improved HER current density (Figure 20d). This high activity compared favorably with previous $MoS_2$ catalysts[77,78] owing to the small size edge-rich $MoS_2$ nanoparticles intimately coupled to the underlying graphene sheets. To gain insight into the possible reaction mechanism on $MoS_2$/rGO hybrid catalyst, we analyzed the Tafel plot derived from the polarization curve and found a Tafel slope of ∼41 mV/decade (Figure 20e). This was the smallest value measured for $MoS_2$-based HER electrocatalysts and suggested electrochemical desorption as the rate-determining step and thus the Volmer−Heyrovsky HER mechanism.[33a] Further, the hybrid electrocatalyst displayed satisfactory stability with little cathodic current loss after 1000 potential cycles between −0.3 and 0.7 V (Figure 20f).

## 9. INVESTIGATION OF THE STRUCTURE AND COUPLING EFFECTS IN HYBRID MATERIALS

While it is desirable to develop catalysts with high reactivity and sufficient stability, it is equally important to characterize the materials down to the atomic scale and understand the structure−property relationship. Not only will this lead to fundamental understanding of materials but also provide guidance to further material design. Below we present characterizations performed to glean the structures and interactions in the strongly coupled inorganic/nanocarbon hybrid materials as well as CNT−graphene complexes.

### 9.1. X-ray absorption near-edge structures (XANES).

XANES is an X-ray absorption spectroscopy technique that probes photoexcitation of electrons from a core level (absorption edge) of an atom to levels within an energy range of ∼50 eV above the absorption edge. It is characterized by intense resonance owing to excitations of core-level electrons to unoccupied orbitals and multiple scattering of the emitted photoelectrons by the geometrical arrangement of neighboring atoms.[79] Therefore, XANES is sensitive to the local chemistry of the atom being detected, which could be used to

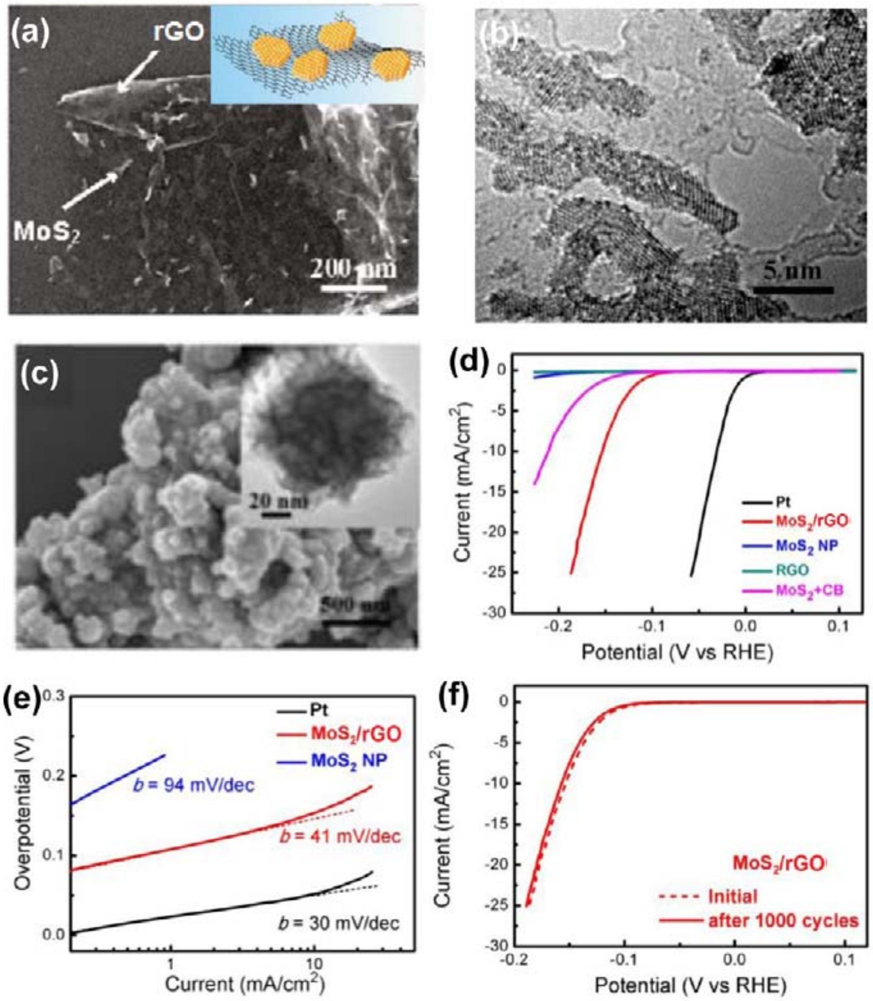

**Figure 20.** (a) SEM and (b) TEM images of the $MoS_2$/rGO hybrid. Inset in (a) shows a schematic representation of the $MoS_2$/rGO hybrid. (c) SEM and TEM (inset) images of the free particles. (d) Polarization curves obtained with several catalysts as indicated and (e) corresponding Tafel plots recorded on glassy carbon electrodes with a catalyst loading of 0.28 mg/cm$^2$. (f) Durability test for the $MoS_2$/rGO hybrid catalyst. Negligible HER current was lost after 1000 cycles from −0.3 to +0.7 V at 100 mV/s. Reproduced with permission from ref 33a. Copyright 2012 American Chemical Society.

investigate the chemical bonding, electronic structure, and interactions of the materials.

We measured XANES at the carbon K-edge to investigate interaction effects to nanocarbon in the hybrid materials. Compared to N-rmGO, the $Co_3O_4$/N-rmGO hybrid showed clear intensity increase of peak at ~288 eV and the nearby shoulders, which are characteristic of defects in graphene associated with nitrogen and oxygen functional groups[80] (Figure 21a). This suggested significantly perturbed bonding between carbon−oxygen and carbon−nitrogen,[81] likely resulted from interfacial Co−O−C and Co−N−C bonds of the oxygen and nitrogen atoms from graphene sheets to metal atoms in the oxide nanoparticles. The $MnCo_2O_4$/N-rmGO[33e] and CoO/NCNT[33g] hybrids showed similar changes in the C K-edge spectra compared to their pure nanocarbon samples (Figure 21b,c), indicating that such bonding is general in the inorganic nanoparticle/nanocarbon hybrids. The metal−N−C bonding could also be gleaned from the nitrogen K-edge XANES. The $MnCo_2O_4$/N-rmGO and $Co_3O_4$/N-rmGO hybrids exhibited higher $\pi^*$ peaks in the range of 398−402 eV and broadened $\sigma^*$ peak at ~407 eV compared to pure N-rmGO in N K-edge XANES (Figure 21d). Enhancement of the $\pi^*$ peak could be attributed to electron transfer away from nitrogen due to coordination of nitrogen to metal in the hybrid,[82] while the broadening of $\sigma^*$ peak suggested strengthened C−N bonding caused by bonding of N-rmGO and metal oxide.[83]

The $Co_3O_4$/N-rmGO hybrid[33b] showed increases in the peak intensities at the Co L-edge XANES compared to pure $Co_3O_4$ nanocrystal (Figure 22a).[84] This was also observed in the metal L-edge XANES of the $MnCo_2O_4$/N-rmGO[33e] and CoO/NCNT[33g] hybrids compared to their respective nanoparticle samples (Figure 22b−d). These results suggested electron transfer from the metal atoms to neighboring atoms in the hybrid materials. A decrease in the unoccupied O 2p−Co 3d hybridized state (~532 eV)[85] was observed in the oxygen K-edge XANES of the $Co_3O_4$/N-rmGO hybrid[33b] compared to $Co_3O_4$ nanoparticles (Figure 23a), likely due to electron transfer from Co to O, giving a higher ionic Co−O bonding in the hybrid.[84]

Metal L-edge XANES were used to investigate the state of metal atom in the hybrid materials. In the Co L-edge XANES, the $MnCo_2O_4$/N-rmGO hybrid showed a lower ratio of high-energy/low-energy peaks than the $Co_3O_4$/N-rmGO hybrid (Figure 23b), suggesting an increase in the ratio of $Co^{2+}/Co^{3+}$

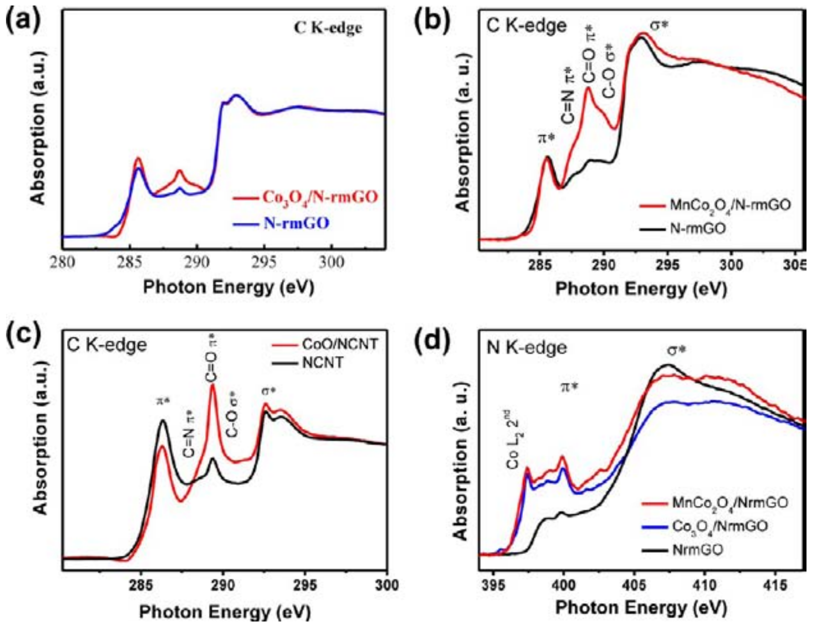

**Figure 21.** (a) C K-edge XANES of the $Co_3O_4$/N-rmGO hybrid and N-rmGO. Reproduced with permission from ref 33b. Copyright 2011 Nature Publishing Group. (b) C K-edge XANES of the $MnCo_2O_4$/N-rmGO hybrid and N-rmGO. Reproduced with permission from ref 33e. Copyright 2012 American Chemical Society. (c) C K-edge XANES of the CoO/NCNT hybrid and NCNT. Reproduced with permission from ref 33g. Copyright 2012 American Chemical Society. (d) N K-edge XANES of the $MnCo_2O_4$/N-rmGO hybrid, the $Co_3O_4$/N-rmGO hybrid and N-rmGO. Reproduced with permission from ref 33e. Copyright 2012 American Chemical Society.

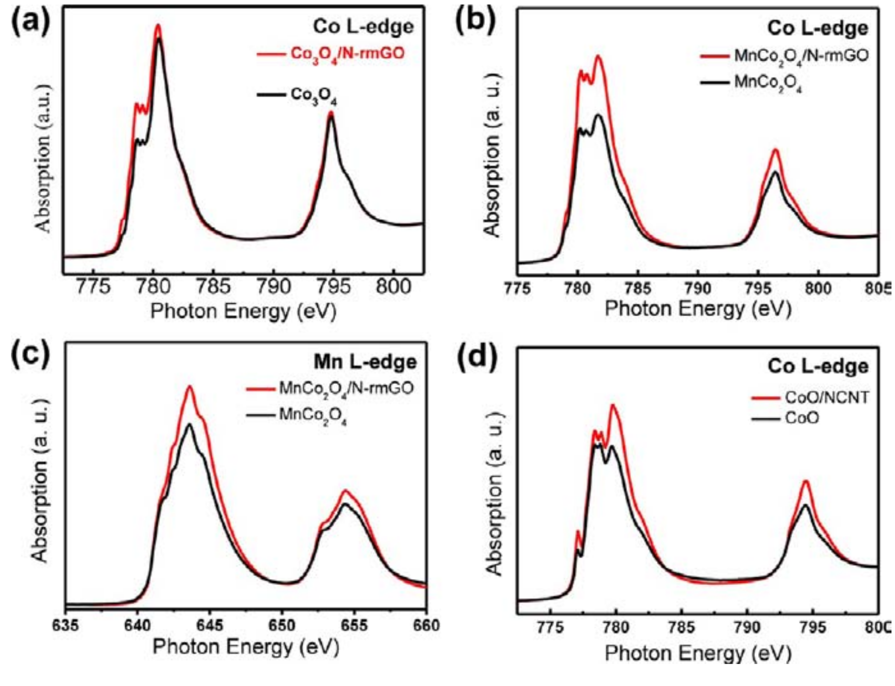

**Figure 22.** (a) Co L-edge XANES of the $Co_3O_4$/N-rmGO hybrid and $Co_3O_4$ nanoparticles. Reproduced with permission from ref 33b. Copyright 2011 Nature Publishing Group. (b) Co L-edge XANES of the $MnCo_2O_4$/N-rmGO hybrid and $MnCo_2O_4$ nanoparticles. (c) Mn L-edge XANES of the $MnCo_2O_4$/N-rmGO hybrid and $MnCo_2O_4$ nanoparticle. Reproduced with permission from ref 33e. Copyright 2012 American Chemical Society. (d) Co L-edge XANES of the CoO/NCNT hybrid and CoO nanoparticles. Reproduced with permission from ref 33e. Copyright 2012 American Chemical Society.

in the $MnCo_2O_4$ hybrid.[86] The Mn L-edge XANES of the $MnCo_2O_4$/N-rmGO hybrid matched that of a $Mn_2O_3$ reference (Figure 23c), indicating Mn was mainly in 3+ state. These results showed $Mn^{3+}$ substitution of $Co^{3+}$ in the oxide particles in the $MnCo_2O_4$ hybrid, resulting a spinel structure of $Co^{II}(Co^{III}Mn^{III})O_4$. $Mn^{3+}$ has been suggested to be a more active ORR catalytic site than Co species,[59] which could account for the higher activity of the $MnCo_2O_4$/N-rmGO hybrid than the $Co_3O_4$/N-rmGO hybrid.[33e]

**9.2. Single-Atom STEM and Energy Loss Spectroscopy.** The most desirable way to characterize a material is to image atom by atom, identify the chemical nature of each atom

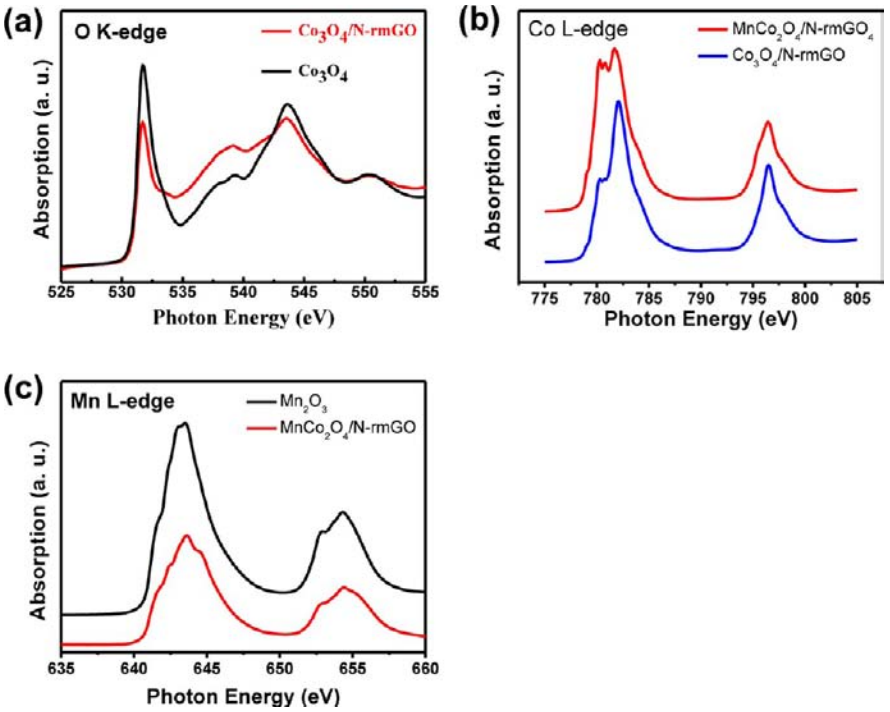

**Figure 23.** (a) O K-edge XANES of $Co_3O_4$ nanoparticles and the $Co_3O_4$/N-rmGO hybrid. Reproduced with permission from ref 33b. Copyright 2011 Nature Publishing Group. (b) Co L-edge XANES of the $MnCo_2O_4$/N-rmGO hybrid and the $Co_3O_4$/N-rmGO hybrid. (c) Mn L-edge XANES of reference $Mn_2O_3$ and the $MnCo_2O_4$/N-rmGO hybrid. Reproduced with permission from ref 33e. Copyright 2012 American Chemical Society.

and reveal the nature of atomic bondings in the material. Graphene presents the thinnest material possible and is highly transparent to the electron beam. This combined with some of the impressive advances in atom-by-atom microscopy imaging and spectroscopy[87] will allow for characterization of catalysts with atomic level information, which would be impossible with traditional catalysts supported on carbon particles.

STEM imaging of a sample performs scanning of a finely focused electron beam in a faster pattern and collecting signal generated pixel by pixel. Aberration-corrected annular dark-field (ADF) imaging and electron energy loss spectroscopy (EELS) in STEM provide powerful tools to interrogate the structural and chemical nature of a material down to the single atom scale. Since the ADF signal is sensitive to the atomic number of the atom,[87a] it is able to differentiate heavier metal atoms from lighter atoms, such as carbon, oxygen, and nitrogen. The identity of elements can be further confirmed by spatially resolved EELS with atomic resolutions.[88] Since ADF and EELS signals are originated from electrons scattered to different solid angles, they can measured simultaneously. The combination of STEM-ADF and EELS mapping is capable of atom-by-atom structural and chemical analysis.

Our collaborators in the Oakridge National Laboratory employed ADF and EELS imaging in STEM to investigate the structure and elemental distribution in our Fe- and N-doped NT-G catalyst (Figure 24a). From ADF images (Figure 24b), bright atoms were found to be dispersed over the carbon background and preferentially located on the nanographene pieces especially along their edges (Figure 24b). EELS analysis corroborated that the brightest atoms were Fe. In addition, the spatial distributions of Fe and N species were mapped out through EELS mapping with nearly atomic precision (Figure 24d,e overlaid with Figure 24f). The distribution of Fe atoms on the nanographene sheets was often accompanied by N atoms, suggesting possible covalently bonded Fe−N species in the material. This was the first time that the chemical nature of metal-N/C type of catalyst was imaged by ADF and EELS at the atomic scale. Although the exact nature of active sites and the role of metal species in metal-N/C ORR catalysts are still unclear,[89] catalysts formed on atomically thin substrates will possess unique structural advantages for direct microscopy spectroscopy investigations, which may eventually lead to an atomic scale and chemical view of the catalyst sites.

## 10. CONCLUSIONS AND OUTLOOK

A series of inorganic/nanocarbon hybrid materials has been developed as efficient electrocatalyst for ORR, OER, and HER. Nanocarbon materials, including graphene and CNT, are oxidized to a suitable degree to introduce functional groups for nucleation, growth, and anchoring of inorganic materials while maintaining a relatively high electrical conductivity. Due to the direct nucleation and growth of inorganic nanomaterials on the functionalized nanocarbon, strong chemical and electrical coupling between the inorganic nanomaterials and nanocarbon is obtained, which enhanced charge transport through interfaces thus affording high electrochemical performance of the hybrid materials.

The strongly coupled hybrid materials represent a new way of synthesis of electrocatalysts. The direct nucleation and growth approach to form hybrid affords intimate coupling and interactions between active materials and carbon supports, leading to both higher electrocatalytic activity and stability than each component alone or their physical mixture. This approach is general to oxides, hydroxides, sulfides, and phosphates and could stimulate further work to improve a wide range of nonprecious metal-based catalysts. The high structural stability of graphene and CNT and strong interactions with inorganic nanomaterials are responsible for the higher stability and

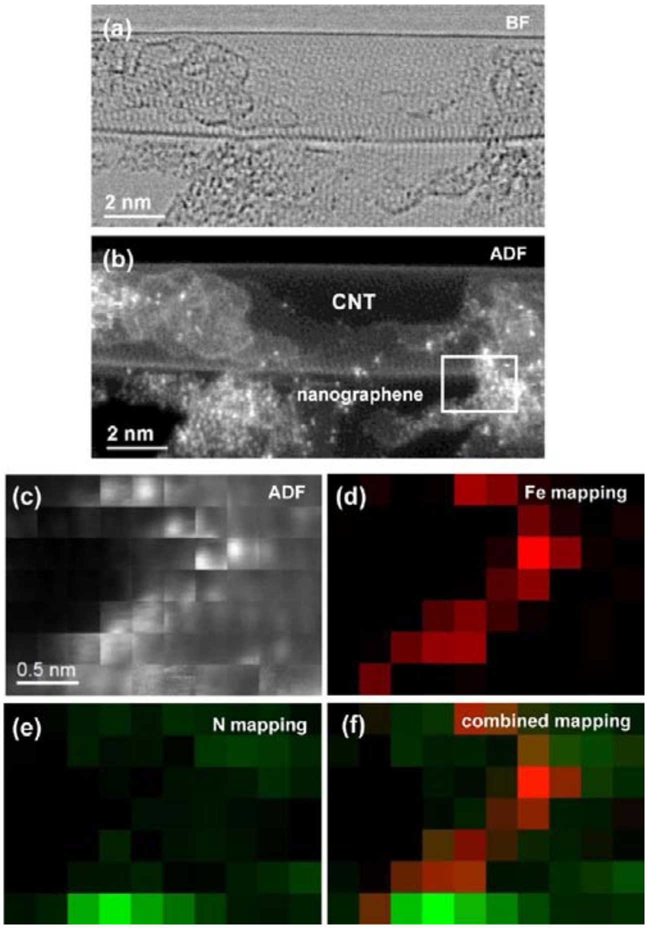

**Figure 24.** (a) Bright-field and (b) simultaneously acquired ADF STEM images of a CNT partially covered with nanosized graphene pieces showing many heavy atoms in the NT-G material. The area marked by the white square in (b) is further characterized by (c) ADF intensity mapping, (d) Fe EELS mapping, (e) N EELS mapping, and (f) overlaid Fe and N EELS maps. The ADF and EELS maps were recorded simultaneously. Reproduced with permission from ref 33d. Copyright 2012 Nature Publishing Group.

durability of the inorganic/nanocarbon hybrids. Catalyst durability is as important as activity for practical application of electrocatalytic systems. The strongly coupled hybrid materials are promising to impart higher stability to renewable energy devices including fuel cells, water splitting by electrolysis, metal-air batteries, and chlor-alkali electrolysis.

Another important feature of the inorganic/nanocarbon synthesis approach is that graphene or CNTs oxidized to various degrees present a novel class of substrate for nanoparticle synthesis. We have observed that the growth of inorganic particles on oxidized nanocarbon substrates often differs from free particle growth in solution. Through the inorganic precursor—carbon substrate interactions, oxidized graphene and nanotubes play important roles in directing the growth of nanoparticles into smaller sizes and interesting shapes (nanoplates, nanorods, etc.). The degree of oxidation of carbon provides a degree of control over the morphology of the nanoparticle. This is interesting and novel from the material chemistry point of views. Last but not least, catalysts formed on nanoscale graphene or CNT structure are unique in that the ultrathin carbon sheets allow for atomic scale interrogation of the catalytic sites formed in these structures by single-atom imaging and spectroscopy. This could present a platform to answer some of the long-standing questions in the electrocatalysis area including natures of catalyst sites.

It is conceivable that the strongly coupled hybrid approach will replace traditional ways of making carbon supported electrocatalysts and other electrochemically active materials to improve batteries, supercapacitors, fuel cells, solar water splitting cells and other types of energy storage and conversion devices. GO can be synthesized from low-cost graphite with high yield, while the production of MWCNT has been advanced to the ton scale at low cost nowadays.[90] The synthesis of inorganic/nanocarbon can be prepared by simple processing methods without incorporation of precious metal. All of these could ensure the low cost of inorganic/nanocarbon hybrid materials for electrocatalysis.

Further work is needed in order for inorganic/nanocarbon hybrids to become a successful class of electrocatalyst material. More efficient catalysts should be developed for a wide variety of electrochemical reactions. There are very few nanocarbon hybrid catalysts for high-performance OER, and hydrogen evolution/oxidation reactions. Little has been explored to improve alcohol oxidation reactions and carbon dioxide reductions. Even for ORR, though several nanocarbon hybrid catalysts have demonstrated good catalytic performance in alkaline and acidic media, there are still significant overpotential gaps to be filled to match that of Pt, especially in acidic conditions. Innovative design of the various components in the hybrid and engineering of the chemical and electrical coupling between inorganics and nanocarbon could further enhance the activity and durability of the electrocatalysts.

More general synthetic chemistry for inorganic/carbon hybrids should be developed to grow a broader range of inorganic nanomaterials and enable better control in the size, phase, and composition of nanoparticles grown on nanocarbon substrates. Size and shape control could enable new hybrid materials with optimized performance. Although our preliminary X-ray spectroscopy studies have revealed possible bonding and covalent interactions in the hybrid materials, it is necessary to improve the understanding and glean the inorganic-carbon interfacial structures at the atomic scale. Such understanding could lead to further optimization of the hybrid materials. It is also important to fully characterize the electrocatalytic properties, i.e., activity and durability of the hybrid materials, and correlate with structures and interfacial coupling of the hybrid. Lastly, for real-world applications, synthetic methods suitable for large scale synthesis should be developed.

## ■ AUTHOR INFORMATION

### Corresponding Author

hdai@stanford.edu

### Notes

The authors declare no competing financial interest.

## ■ ACKNOWLEDGMENTS

This work was supported by a Stinehart Grant for Energy Research at Stanford from the Stanford Precourt Institute for Energy, Intel, Amperex Technology Limited (ATL), U.S. Department of Energy and Office of Naval Research. X-ray spectroscopy is done at CLS supported by the NSERC, NRC, CIHR of Canada, the Province of Saskatchewan, WEDC, and the University of Saskatchewan. We are grateful to our collaborators Drs. Jigang Zhou, Jian Wang, Steven J. Pennycook and Fei Wei.

## ■ REFERENCES

(1) Lota, G.; Fic, K.; Frackowiak, E. *Energy Environ. Sci.* **2011**, *4*, 1592−1605.

(2) Seger, B.; Kamat, P. V. *J. Phys. Chem. C* **2009**, *113*, 7990−7995.

(3) Kunze, J.; Stimming, U. *Angew. Chem., Int. Ed.* **2009**, *48*, 9230−9237.

(4) Kordesch, K. V.; Simader, G. R. *Chem. Rev.* **1995**, *95*, 191−207.

(5) Dante, R. C.; Menzl, F.; Lehmann, J.; Sponholz, C.; Luschtinetz, O.; Solorza-Feria, O. *J. Appl. Electrochem.* **2006**, *36*, 187−193.

(6) (a) Chen, J.; Lim, B.; Lee, E. P.; Xia, Y. *Nano Today* **2009**, *4*, 81−95. (b) Antolini, E. *Energy Environ. Sci.* **2009**, *2*, 915−931. (c) Trasatti, S. *Electrodes of Conductive Metal Oxides*; Elsevier: Amsterdam, 1980.

(7) (a) Armand, M.; Tarascon, J. M. *Nature* **2008**, *451*, 652−657. (b) Moussallem, I.; Jorissen, J.; Kunz, U.; Pinnow, S.; Turek, T. *J. Appl. Electrochem.* **2008**, *38*, 1177−1194.

(8) (a) Stamenkovic, V.; Mun, B. S.; Mayrhofer, K. J. J.; Ross, P. N.; Markovic, N. M.; Rossmeisl, J.; Greeley, J.; Norskov, J. K. *Angew. Chem., Int. Ed.* **2006**, *45*, 2897−2901. (b) Srivastava, R.; Mani, P.; Hahn, N.; Strasser, P. *Angew. Chem., Int. Ed.* **2007**, *46*, 8988−8991. (c) Morozan, A.; Jousselme, B.; Palacin, S. *Energy Environ. Sci.* **2011**, *4*, 1238−1254.

(9) (a) Lefevre, M.; Proietti, E.; Jaouen, F.; Dodelet, J.-P. *Science* **2009**, *324*, 71−74. (b) Meng, H.; Jaouen, F.; Proietti, E.; Lefevre, M.; Dodelet, J. P. *Electrochem. Commun.* **2009**, *11*, 1986−1989. (c) Gang, W.; More, K. L.; Johnston, C. M.; Zelenay, P. *Science* **2011**, 332. (d) Piana, M.; Catanorchi, S.; Gasteiger, H. A. *Electrochem. Soc. Trans.* **2008**, *16*, 2045−2055.

(10) Gao, M.-R.; Jiang, J.; Yu, S.-H. *Small* **2012**, *8*, 13−27.

(11) (a) Meadowcroft, D. B. *Nature* **1970**, *226*, 847−848. (b) Suntivich, J.; Gasteiger, H. A.; Yabuuchi, N.; Nakanishi, H.; Goodenough, J. B.; Shan-Horn, Y. *Nat. Chem.* **2011**, *3*, 546−550.

(12) (a) Sugawara, M.; Ohno, M.; Matsuki, K. *J. Mater. Chem.* **1997**, *7*, 833−836. (b) Cheng, F.; Shen, J.; Peng, B.; Pan, Y.; Tao, Z.; Chen, J. *Nat. Chem.* **2011**, *3*, 79−84.

(13) (a) Gong, K.; Du, F.; Xia, Z.; Durstock, M.; Dai, L. *Science* **2009**, *323*, 760−764. (b) Liu, R.; Wu, D.; Feng, X.; Muellen, K. *Angew. Chem., Int. Ed.* **2010**, *49*, 2565−2569. (c) Su, D. S.; Zhang, J.; Frank, B.; Thomas, A.; Wang, X.; Paraknowitsch, J.; Schloegl, R. *ChemSusChem* **2010**, *3*, 169−180.

(14) Gewirth, A. A.; Thorum, M. S. *Inorg. Chem.* **2010**, *49*, 3557−3566.

(15) (a) Walter, M. G.; Warren, E. L.; McKone, J. R.; Boettcher, S. W.; Mi, Q.; Santori, E. A.; Lewis, N. S. *Chem. Rev.* **2010**, *110*, 6446−6473. (b) Kudo, A.; Miseki, Y. *Chem. Soc. Rev.* **2009**, *38*, 253−278. (c) Gray, H. B. *Nat. Chem.* **2009**, *1*, 112−112.

(16) (a) Cheng, F. Y.; Chen, J. *Chem. Soc. Rev.* **2012**, *41*, 2172−2192. (b) Lu, Y. C.; Xu, Z. C.; Gasteiger, H. A.; Chen, S.; Hamad-Schifferli, K.; Shao-Horn, Y. *J. Am. Chem. Soc.* **2010**, *132*, 12170−12171.

(17) (a) Koper, M. T. M. *J. Electroanal. Chem.* **2011**, *660*, 254−260. (b) Kanan, M. W.; Nocera, D. G. *Science* **2008**, *321*, 1072−1075.

(18) Lee, Y.; Suntivich, J.; May, K. J.; Perry, E. E.; Shao-Horn, Y. *J. Phys. Chem. Lett.* **2012**, *3*, 399−404.

(19) (a) Esswein, A. J.; McMurdo, M. J.; Ross, P. N.; Bell, A. T.; Tilley, T. D. *J. Phys. Chem. C* **2009**, *113*, 15068. (b) Li, Y. G.; Hasin, P.; Wu, Y. Y. *Adv. Mater.* **2010**, *22*, 1926−1929. (c) Liang, Y. Y.; Li, Y. G.; Wang, H. L.; Zhou, J. G.; Wang, J.; Regier, T.; Dai, H. J. *Nat. Mater.* **2011**, *10*, 780−786. (d) Gorlin, Y.; Jaramillo, T. F. *J. Am. Chem. Soc.* **2010**, *132*, 13612−13614. (e) Cui, B.; Lin, H.; Li, J. B.; Li, X.; Yang, J.; Tao, J. *Adv. Funct. Mater.* **2008**, *18*, 1440.

(20) (a) Bockris, J. O.; Otagawa, T. *J. Electrochem. Soc.* **1984**, *131*, 290−302. (b) Suntivich, J.; May, K. J.; Gasteiger, H. A.; Goodenough, J. B.; Shao-Horn, Y. *Science* **2011**, *334*, 1383−1385.

(21) Markovic, N. M.; Ross, P. N. *Surf. Sci. Rep.* **2002**, *45*, 121−229.

(22) Camara, G. A.; Ticianelli, E. A.; Mukerjee, S.; Lee, S. J.; McBreen, J. *J. Electrochem. Soc.* **2002**, *149*, A748−A753.

(23) Jaramillo, T. F.; Jorgensen, K. P.; Bonde, J.; Nielsen, J. H.; Horch, S.; Chorkendorff, I. *Science* **2007**, *317*, 100−102.

(24) Esposito, D. V.; Hunt, S. T.; Stottlemyer, A. L.; Dobson, K. D.; McCandless, B. E.; Birkmire, R. W.; Chen, J. G. *Angew. Chem., Int. Ed.* **2010**, *49*, 9859−9862.

(25) Helm, M. L.; Stewart, M. P.; Bullock, R. M.; DuBois, M. R.; DuBois, D. L. *Science* **2011**, *333*, 863−866.

(26) McKone, J. R.; Warren, E. L.; Bierman, M. J.; Boettcher, S. W.; Brunschwig, B. S.; Lewis, N. S.; Gray, H. B. *Energy Environ. Sci.* **2011**, *4*, 3573−3583.

(27) Yu, E. H.; Krewer, U.; Scott, K. *Energies* **2010**, *3*, 1499−1528.

(28) Li, C. W.; Kanan, M. W. *J. Am. Chem. Soc.* **2012**, *134*, 7231−7234.

(29) Sharma, S.; Pollet, B. G. *J. Power Sources* **2012**, *208*, 96−119.

(30) Antolini, E. *Appl. Catal., B* **2009**, *88*, 1−24.

(31) Geng, D. S.; Chen, Y.; Chen, Y. G.; Li, Y. L.; Li, R. Y.; Sun, X. L.; Ye, S. Y.; Knights, S. *Energy Environ. Sci.* **2011**, *4*, 760−764.

(32) Lee, J.-S.; Park, G. S.; Lee, H. I.; Kim, S. T.; Cao, R.; Liu, M.; Cho, J. *Nano Lett.* **2011**, *11*, 5362−5366.

(33) (a) Li, Y.; Wang, H.; Xie, L.; Liang, Y.; Hong, G.; Dai, H. *J. Am. Chem. Soc.* **2011**, *133*, 7296−7299. (b) Liang, Y.; Li, Y.; Wang, H.; Zhou, J.; Wang, J.; Regier, T.; Dai, H. *Nat. Mater.* **2011**, *10*, 780−786. (c) Wang, H.; Liang, Y.; Li, Y.; Dai, H. *Angew. Chem., Int. Ed.* **2011**, *50*, 10969−10972. (d) Li, Y.; Zhou, W.; Wang, H.; Xie, L.; Liang, Y.; Wei, F.; Idrobo, J.-C.; Pennycook, S. J.; Dai, H. *Nat Nano* **2012**, *7*, 394−400. (e) Liang, Y.; Wang, H.; Zhou, J.; Li, Y.; Wang, J.; Regier, T.; Dai, H. *J. Am. Chem. Soc.* **2012**, *134*, 3517−3523. (f) Feng, J.; Liang, Y.; Wang, H.; Li, Y.; Zhang, B.; Zhou, J.; Wang, J.; Regier, T.; Dai, H. *Nano Res.* **2012**, *5*, 718−725. (g) Liang, Y.; Wang, H. D.; Peng; Chang, W.; Hong, G.; Li, Y.; Gong, M.; Xie, L.; Zhou, J.; Wang, J.; Regier, T. Z.; Wei, F.; Dai, H. *J. Am. Chem. Soc.* **2012**, *134*, 15849−15857.

(34) (a) Zhang, Y.; Franklin, N. W.; Chen, R. J.; Dai, H. J. *Chem. Phys. Lett.* **2000**, *331*, 35−41. (b) Lu, Y. R.; Bangsaruntip, S.; Wang, X. R.; Zhang, L.; Nishi, Y.; Dai, H. J. *J. Am. Chem. Soc.* **2006**, *128*, 3518−3519. (c) Wang, X.; Tabakman, S. M.; Dai, H. *J. Am. Chem. Soc.* **2008**, *130*, 8152−8153.

(35) (a) Guo, S. J.; Dong, S. J. *Chem. Soc. Rev.* **2011**, *40*, 2644−2672. (b) Sgobba, V.; Guldi, D. M. *Chem. Soc. Rev.* **2009**, *38*, 165−184.

(36) (a) Wang, H.; Cui, L.-F.; Yang, Y.; Casalongue, H. S.; Robinson, J. T.; Liang, Y.; Cui, Y.; Dai, H. *J. Am. Chem. Soc.* **2010**, *132*, 13978−13980. (b) Wang, H.; Yang, Y.; Liang, Y.; Cui, L.-F.; Casalongue, H. S.; Li, Y.; Hong, G.; Cui, Y.; Dai, H. *Angew. Chem., Int. Ed.* **2011**, *50*, 7364−7368. (c) Wang, H.; Liang, Y.; Gong, M.; Li, Y.; Chang, W.; Mefford, T.; Zhou, J.; Wang, J.; Regier, T.; Wei, F.; Dai, H. *Nat. Commun.* **2012**, 3. (d) Wang, H.; Yang, Y.; Liang, Y.; Robinson, J. T.; Li, Y.; Jackson, A.; Cui, Y.; Dai, H. *Nano Lett.* **2011**, *11*, 2644−2647.

(37) (a) Wang, H.; Casalongue, H. S.; Liang, Y.; Dai, H. *J. Am. Chem. Soc.* **2010**, *132*, 7472−7477. (b) Wang, H.; Liang, Y.; Mirfakhrai, T.; Chen, Z.; Casalongue, H. S.; Dai, H. *Nano Res.* **2011**, *4*, 729−736.

(38) (a) Park, S.; Shao, Y. Y.; Wan, H. Y.; Rieke, P. C.; Viswanathan, V. V.; Towne, S. A.; Saraf, L. V.; Liu, J.; Lin, Y. H.; Wang, Y. *Electrochem. Commun.* **2011**, *13*, 258−261. (b) Tang, H.; Chen, J. H.; Huang, Z. P.; Wang, D. Z.; Ren, Z. F.; Nie, L. H.; Kuang, Y. F.; Yao, S. Z. *Carbon* **2004**, *42*, 191−197.

(39) (a) Shao, Y. Y.; Zhang, S.; Engelhard, M. H.; Li, G. S.; Shao, G. C.; Wang, Y.; Liu, J.; Aksay, I. A.; Lin, Y. H. *J. Mater. Chem.* **2010**, *20*, 7491−7496. (b) Qu, L.; Liu, Y.; Baek, J.-B.; Dai, L. *ACS Nano* **2010**, *4*, 1321−1326.

(40) Hamdani, M.; Singh, R. N.; Chartier, P. *Int. J. Electrochem. Sci.* **2010**, *5*, 556−577.

(41) Singh, R. N.; Pandey, J. P.; Singh, N. K.; Lal, B.; Chartier, P.; Koenig, J. F. *Electrochim. Acta* **2000**, *45*, 1911−1919.

(42) Eder, D. *Chem. Rev.* **2010**, *110*, 1348−1385.

(43) Liu, J.; Rinzler, A. G.; Dai, H. J.; Hafner, J. H.; Bradley, R. K.; Boul, P. J.; Lu, A.; Iverson, T.; Shelimov, K.; Huffman, C. B.; Rodriguez-Macias, F.; Shon, Y. S.; Lee, T. R.; Colbert, D. T.; Smalley, R. E. *Science* **1998**, *280*, 1253−1256.

(44) Holzinger, M.; Vostrowsky, O.; Hirsch, A.; Hennrich, F.; Kappes, M.; Weiss, R.; Jellen, F. *Angew. Chem., Int. Ed.* **2001**, *40*, 4002−4005.

(45) Bahr, J. L.; Yang, J. P.; Kosynkin, D. V.; Bronikowski, M. J.; Smalley, R. E.; Tour, J. M. *J. Am. Chem. Soc.* **2001**, *123*, 6536−6542.

(46) Hummers, W. S.; Offeman, R. E. *J. Am. Chem. Soc.* **1958**, *80*, 1339−1339.

(47) (a) Wang, H.; Dai, H. *Chem. Soc. Rev.* **2013**, DOI: 10.1039/C2CS35307E. (b) Gao, W.; Alemany, L. B.; Ci, L.; Ajayan, P. M. *Nat. Chem.* **2009**, *1*, 403−408. (c) Park, S.; Ruoff, R. S. *Nat. Nanotechnol.* **2009**, *4*, 217−224.

(48) Sun, X.; Liu, Z.; Welsher, K.; Robinson, J. T.; Goodwin, A.; Zaric, S.; Dai, H. *Nano Res.* **2008**, *1*, 203−212.

(49) Han, W. Q.; Zettl, A. *Nano Lett.* **2003**, *3*, 681−683.

(50) Park, J. H.; Ko, J. M.; Park, O. O. *J. Electrochem. Soc.* **2003**, *150*, A864−A867.

(51) Shan, Y.; Gao, L. *Chem. Lett.* **2004**, *33*, 1560−1561.

(52) Wang, H. L.; Casalongue, H. S.; Liang, Y. Y.; Dai, H. J. *J. Am. Chem. Soc.* **2010**, *132*, 7472−7477.

(53) Liang, Y.; Wang, H.; Casalongue, H. S.; Chen, Z.; Dai, H. *Nano Res.* **2010**, *3*, 701−705.

(54) Wang, H.; Robinson, J. T.; Diankov, G.; Dai, H. *J. Am. Chem. Soc.* **2010**, *132*, 3270−3271.

(55) Moussallem, I.; Joerissen, J.; Kunz, U.; Pinnow, S.; Turek, T. *J. Appl. Electrochem.* **2008**, *38*, 1177−1194.

(56) Spendelow, J. S.; Wieckowski, A. *Phys. Chem. Chem. Phys.* **2007**, *9*, 2654−2675.

(57) Dong, Y.; He, K.; Yin, L.; Zhang, A. *Nanotechnology* **2007**, *18*, 435602.

(58) Bidault, F.; Brett, D. J. L.; Middleton, P. H.; Brandon, N. P. *J. Power Sources* **2009**, *187*, 39−48.

(59) De Koninck, M.; Marsan, B. *Electrochim. Acta* **2008**, *53*, 7012−7021.

(60) Genies, L.; Bultel, Y.; Faure, R.; Durand, R. *Electrochim. Acta* **2003**, *48*, 3879−3890.

(61) (a) Mao, L. Q.; Zhang, D.; Sotomura, T.; Nakatsu, K.; Koshiba, N.; Ohsaka, T. *Electrochim. Acta* **2003**, *48*, 1015−1021. (b) Cheng, F.; Su, Y.; Liang, J.; Tao, Z.; Chen, J. *Chem. Mater.* **2010**, *22*, 898−905. (c) Gorlin, Y.; Jaramillo, T. F. *J. Am. Chem. Soc.* **2010**, *132*, 13612−13614. (d) Xiao, W.; Wang, D.; Lou, X. W. *J. Phys. Chem. C.* **2010**, *114*, 1694−1700. (e) Benbow, E. M.; Kelly, S. P.; Zhao, L.; Reutenauer, J. W.; Suib, S. L. *J. Phys. Chem. C.* **2011**, *115*, 22009−22017. (f) Garcia, A. C.; Herrera, A. D.; Ticianelli, E. A.; Chatenet, M.; Poinsignon, C. *J. Electrochem. Soc.* **2011**, *158*, B290−B296. (g) Lee, J.-S.; Lee, T.; Song, H.-K.; Cho, J.; Kim, B.-S. *Energ. Environ. Sci.* **2011**, *4*, 4148−4154. (h) Yang, Z.; Zhou, X.; Nie, H.; Yao, Z.; Huang, S. *ACS Appl. Mater. Interfaces* **2011**, *3*, 2601−2606. (i) Lima, F. H. B.; Calegaro, M. L.; Ticianelli, E. A. *Electrochim. Acta* **2007**, *52*, 3732−3738. (j) Lima, F. H. B.; Calegaro, M. L.; Ticianelli, E. A. *J. Electroanal. Chem.* **2006**, *590*, 152−160.

(62) Winter, M.; Brodd, R. J. *Chem. Rev.* **2004**, *104*, 4245−4269.

(63) Debe, M. K. *Nature* **2012**, *486*, 43−51.

(64) Chen, Z.; Higgins, D.; Yu, A.; Zhang, L.; Zhang, J. *Energy Environ. Sci.* **2011**, *4*, 3167−3192.

(65) (a) Feng, Y.; He, T.; Alonso-Vante, N. *Chem. Mater.* **2008**, *20*, 26−28. (b) Zhu, L.; Susac, D.; Teo, M.; Wong, K. C.; Wong, P. C.; Parsons, R. R.; Bizzotto, D.; Mitchell, K. A. R.; Campbell, S. A. *J. Catal.* **2008**, *258*, 235−242. (c) Alonso-Vante, N. *ChemPhysChem* **2010**, *11*, 2732−2744. (d) Feng, Y. J.; He, T.; Alonso-Vante, N. *Fuel Cells* **2010**, *10*, 77−83.

(66) Wang, H.; Liang, Y.; Li, Y.; Chang, W.; Dai, H., in preparation.

(67) Wu, G.; More, K. L.; Johnston, C. M.; Zelenay, P. *Science* **2011**, *332*, 443−447.

(68) Jaouen, F.; Proietti, E.; Lefevre, M.; Chenitz, R.; Dodelet, J.-P.; Wu, G.; Chung, H. T.; Johnston, C. M.; Zelenay, P. *Energy Environ. Sci.* **2011**, *4*, 114−130.

(69) (a) Yang, J.; Liu, D.-J.; Kariuki, N. N.; Chen, L. X. *Chem. Commun.* **2008**, 329−331. (b) Geng, D.; Liu, H.; Chen, Y.; Li, R.; Sun, X.; Ye, S.; Knights, S. *J. Power Sources* **2011**, *196*, 1795−1801. (c) Kundu, S.; Nagaiah, T. C.; Xia, W.; Wang, Y.; Van Dommele, S.; Bitter, J. H.; Santa, M.; Grundmeier, G.; Bron, M.; Schuhmann, W.; Muhler, M. *J. Phys. Chem. C* **2009**, *113*, 14302−14310. (d) Xiong, W.; Du, F.; Liu, Y.; Perez, A.; Supp, M.; Ramakrishnan, T. S.; Dai, L.; Jiang, L. *J. Am. Chem. Soc.* **2010**, *132*, 15839−15841. (e) Yu, D.; Zhang, Q.; Dai, L. *J. Am. Chem. Soc.* **2010**, *132*, 15127−15129.

(70) Meng, H.; Jaouen, F.; Proietti, E.; Lefevre, M.; Dodelet, J.-P. *Electrochem. Commun.* **2009**, *11*, 1986−1989.

(71) Esswein, A. J.; McMurdo, M. J.; Ross, P. N.; Bell, A. T.; Tilley, T. D. *J. Phys. Chem. C* **2009**, *113*, 15068−15072.

(72) Wang, H.; Yang, Y.; Liang, Y.; Zheng, G.; Li, Y.; Cui, Y.; Dai, H. *Energy Environ. Sci.* **2012**, *5*, 7931−7935.

(73) (a) Bruce, P. G.; Freunberger, S. A.; Hardwick, L. J.; Tarascon, J. M. *Nat. Mater.* **2012**, *11*, 19−29. (b) Girishkumar, G.; McCloskey, B.; Luntz, A. C.; Swanson, S.; Wilcke, W. *J. Phys. Chem. Lett.* **2010**, *1*, 2193−2203. (c) Lee, J. S.; Kim, S. T.; Cao, R.; Choi, N. S.; Liu, M.; Lee, K. T.; Cho, J. *Adv. Energy Mater.* **2011**, *1*, 34−50.

(74) (a) Debart, A.; Bao, J.; Armstrong, G.; Bruce, P. G. *J. Power Sources* **2007**, *174*, 1177−1182. (b) Lu, Y. C.; Xu, Z. C.; Gasteiger, H. A.; Chen, S.; Hamad-Schifferli, K.; Shao-Horn, Y. *J. Am. Chem. Soc.* **2010**, *132*, 12170−12171. (c) Li, Y. L.; Wang, J. J.; Li, X. F.; Geng, D. S.; Li, R. Y.; Sun, X. L. *Chem. Commun.* **2011**, *47*, 9438−9440. (d) Li, Y. L.; Wang, J. J.; Li, X. F.; Liu, J.; Geng, D. S.; Yang, J. L.; Li, R. Y.; Sun, X. L. *Electrochem. Commun.* **2011**, *13*, 668−672.

(75) (a) Freunberger, S. A.; Chen, Y. H.; Peng, Z. Q.; Griffin, J. M.; Hardwick, L. J.; Barde, F.; Novak, P.; Bruce, P. G. *J. Am. Chem. Soc.* **2011**, *133*, 8040−8047. (b) Xu, W.; Xu, K.; Viswanathan, V. V.; Towne, S. A.; Hardy, J. S.; Xiao, J.; Hu, D. H.; Wang, D. Y.; Zhang, J. G. *J. Power Sources* **2011**, *196*, 9631−9639. (c) Xiao, J.; Hu, J. Z.; Wang, D. Y.; Hu, D. H.; Xu, W.; Graff, G. L.; Nie, Z. M.; Liu, J.; Zhang, J. G. *J. Power Sources* **2011**, *196*, 5674−5678.

(76) Chen, Z.; Kibsgaard, J.; Jaramillo, T. F. *Proc. SPIE* **2010**, *7770*, 77700K/77701−77700K/77707.

(77) (a) Hinnemann, B.; Moses, P. G.; Bonde, J.; Jorgensen, K. P.; Nielsen, J. H.; Horch, S.; Chorkendorff, I.; Norskov, J. K. *J. Am. Chem. Soc.* **2005**, *127*, 5308−5309. (b) Jaramillo, T. F.; Jorgensen, K. P.; Bonde, J.; Nielsen, J. H.; Horch, S.; Chorkendorff, I. *Science* **2007**, *317*, 100−102. (c) Bonde, J.; Moses, P. G.; Jaramillo, T. F.; Norskov, J. K.; Chorkendorff, I. *Faraday Discuss.* **2008**, *140*, 219−231.

(78) Jaramillo, T. F.; Bonde, J.; Zhang, J.; Ooi, B.-L.; Andersson, K.; Ulstrup, J.; Chorkendorff, I. *J. Phys. Chem. C* **2008**, *112*, 17492−17498.

(79) (a) Kruse, J.; Leinweber, P.; Eckhardt, K.-U.; Godlinski, F.; Hu, Y.; Zuin, L. *J. Synchrotron Radiat.* **2009**, *16*, 247−259. (b) Yang, S.; Wang, D.; Liang, G.; Yiu, Y. M.; Wang, J.; Liu, L.; Sun, X.; Sham, T.-K. *Energy Environ. Sci.* **2012**, *5*, 7007−7016.

(80) (a) Zhang, L.-S.; Liang, X.-Q.; Song, W.-G.; Wu, Z.-Y. *Phys. Chem. Chem. Phys.* **2010**, *12*, 12055−12059. (b) Zhou, J. G.; Fang, H. T.; Hu, Y. F.; Sham, T. K.; Wu, C. X.; Liu, M.; Li, F. *J. Phys. Chem. C* **2009**, *113*, 10747−10750.

(81) (a) Zhou, J.; Wang, J.; Fang, H.; Sham, T.-K. *J. Mater. Chem.* **2011**, *21*, 5944−5949. (b) Zhang, L.-S.; Liang, X.-Q.; Song, W.-G.; Wu, Z.-Y. *Phys. Chem. Chem. Phys.* **2010**, *12*, 12055−12059.

(82) Kelly, D. N.; Schwartz, C. P.; Uejio, J. S.; Duffin, A. M.; England, A. H.; Saykally, R. J. *J. Chem. Phys.* **2010**, 133.

(83) Zhou, J.; Zhou, X.; Li, R.; Sun, X.; Ding, Z.; Cutler, J.; Sham, T.-K. *Chem. Phys. Lett.* **2009**, *474*, 320−324.

(84) Zhou, J. G.; Fang, H. T.; Maley, J. M.; Murphy, M. W.; Peter, Ko, J. Y.; Cutler, J. N.; Sammynaiken, R.; Sham, T. K.; Liu, M.; Li, F. *J. Mater. Chem.* **2009**, *19*, 6804−6809.

(85) Rojas, T. C.; Sanchez-Lopez, J. C.; Sayagues, M. J.; Reddy, E. P.; Caballero, A.; Fernandez, A. *J. Mater. Chem.* **1999**, *9*, 1011−1017.

(86) Zheng, F.; Alayoglu, S.; Guo, J.; Pushkarev, V.; Li, Y.; Glans, P.-A.; Chen, J.-l.; Somorjai, G. *Nano Lett.* **2011**, *11*, 847−853.

(87) (a) Krivanek, O. L.; Chisholm, M. F.; Nicolosi, V.; Pennycook, T. J.; Corbin, G. J.; Dellby, N.; Murfitt, M. F.; Own, C. S.; Szilagyi, Z. S.; Oxley, M. P.; Pantelides, S. T.; Pennycook, S. J. *Nature* **2010**, *464*, 571−574. (b) Varela, M.; Gazquez, J.; Pennycook, S. J. *MRS Bull.* **2012**, *37*, 29−35.

(88) Hunt, J. A.; Williams, D. B. *Ultramicroscopy* **1991**, *38*, 47−73.

(89) (a) Scherson, D. A.; Yao, S. B.; Yeager, E. B.; Eldridge, J.; Kordesch, M. E.; Hoffman, R. W. *J. Phys. Chem.* **1983**, *87*, 932−943. (b) Lefevre, M.; Dodelet, J. P.; Bertrand, P. *J. Phys. Chem. B* **2002**, *106*, 8705−8713. (c) Thorum, M. S.; Hankett, J. M.; Gewirth, A. A. *J. Phys. Chem. Lett.* **2011**, 2.

(90) Kumar, M.; Ando, Y. *J. Nanosci. Nanotechnol.* **2010**, *10*, 3739−3758.